

# Physics-based GPS data inversion to estimate three-dimensional elastic and inelastic strain fields

Akemi Noda\* and Mitsuhiro Matsu'ura†

Department of Earth and Planetary Science, University of Tokyo, Bunkyo-ku, Tokyo 113-0033, Japan. E-mail: akemi-noda@kke.co.jp

Accepted 2010 March 29. Received 2010 February 16; in original form 2009 August 12

## SUMMARY

The Earth's crust is macroscopically treated as a linear elastic body, but it includes a number of defects. The occurrence of inelastic deformation such as brittle fracture at the defects brings about elastic deformation in the surrounding regions. The crustal deformation observed through geodetic measurements is the sum of the inelastic deformation as source and the elastic deformation as effect. On such a basic idea, we created a theory of physics-based strain analysis with general source representation by moment tensor, and developed an inversion method to separately estimate 3-D elastic and inelastic strain fields from GPS data. In this method, first, the optimum distribution of moment density tensor is determined from observed GPS data by using Akaike's information criterion. Then, the elastic and inelastic strain fields are obtained from the optimum moment tensor distribution by theoretical computation and direct conversion with elastic compliance tensor, respectively. We applied the inversion method to GPS horizontal velocity data, and succeeded in separately estimating 3-D elastic and inelastic strain rate fields in the Niigata–Kobe transformation zone, central Japan. As for the surface patterns of total strain, the present results of 3-D physics-based inversion analysis accord with the previous results of 2-D geometric inversion analysis. From the 3-D patterns of the inverted elastic and inelastic strain fields, we revealed that the remarkable horizontal contraction in the Niigata–Kobe transformation zone is elastic and restricted near the surface, but the remarkable shear deformation is inelastic and extends over the upper crust.

**Key words:** Inverse theory; Space geodetic surveys; Elasticity and anelasticity; Intraplate processes; High strain deformation zones.

## 1 INTRODUCTION

Surface deformation of the Earth's crust is now directly observable through GPS measurements. However, to understand the mechanism of crustal deformation, we need to know 3-D elastic and inelastic strain-rate fields separately. In general, the deformation of continuum is completely described by the nine independent elements of deformation gradient tensor. Since GPS measurements are restricted to the Earth's surface, unfortunately, three vertical gradients of displacement vectors are unobservable. Therefore, in conventional geometric strain analysis, we can only estimate 2-D horizontal strain components. In addition, the rational separation of crustal strain into elastic and inelastic parts has been left as an unsolved problem (e.g. Reilly 2003).

The Earth's crust is basically a linear elastic body, but it includes a number of defects, and so the mechanism of crustal deforma-

tion is complex. From a microscopic point of view, the mode of rock deformation can be classified into elastic deformation, brittle fracture and plastic flow. Elastic deformation is reversible, whereas brittle fracture and plastic flow are irreversible, which proceed so as to release the potential energy of the total system. The essential difference between brittle fracture and plastic flow is only in the manner of development; that is, the former is unstable and the latter is stable. Practically, we cannot distinguish them without direct observation of dynamic processes (Kostrov 1974; Twiss & Unruh 1998). Therefore, from a macroscopic point of view, we may classify the mode of crustal deformation into elastic deformation and inelastic deformation. Here, it should be noted that the occurrence of inelastic deformation at defects inevitably brings about elastic deformation in the surrounding regions.

So far crustal deformation has been treated as a 2-D problem in two different ways; mostly in the geometric analysis of geodetic data (e.g. Tsuboi 1932; Frank 1966; Shen *et al.* 1996; El-Fiky & Kato 1999) and occasionally in the physical analysis of earthquake and/or active fault data (e.g. Wesnousky *et al.* 1982; Jackson & McKenzie 1988; Holt & Haines 1993) based on the concept of Kostrov's seismic moment tensor (Kostrov 1974). The essential difference between the geometric analysis and the physical analysis is

\*Now at: Kozo Keikaku Engineering Inc., Nakano-ku, Tokyo 164-0011, Japan.

†Now at: Institute of Statistical Mathematics, Tachikawa, Tokyo 190-8562, Japan.

in the meaning of estimated crustal deformation: the former gives the sum of the elastic and inelastic deformation, whereas the latter gives the purely inelastic deformation.

From the geometric analysis of interseismic horizontal velocity data, obtained by the nationwide continuous GPS array operated by the Geographical Survey Institute of Japan, Kato *et al.* (1998), Sagiya *et al.* (2000) and Mazzotti *et al.* (2001) have independently estimated horizontal strain-rate fields in Japanese Islands, and revealed the existence of inland high strain-rate zones, which cannot be explained by elastic deformation due to mechanical interaction at plate interfaces. Mazzotti *et al.* (2001), Townend & Zoback (2006) and El-Fiky & Kato (2006) have computed the difference of the observed deformation field from the elastic deformation field due to plate-to-plate interaction, and considered it to be the inelastic part of deformation field. However, their approach is logically inconsistent, because inelastic deformation in the crust inevitably causes elastic deformation in the surrounding region.

On the other hand, from the physical analysis of earthquakes and Quaternary active faults based on Kostrov's relation between seismic moment tensors and deformation rates, Wesnousky *et al.* (1982) and Shen-Tu *et al.* (1995) have estimated crustal deformation rates in Japanese Islands. In these studies, however, the elastic part of crustal deformation is completely ignored, because the deformation estimated from the physical analysis is purely inelastic.

In Section 2 of this paper, regarding the Earth's crust as a linear elastic body including a number of defects, and representing the source of crustal deformation by moment tensor, we create a theory of physics-based strain analysis, which can resolve the long outstanding problem for separate estimation of 3-D elastic and inelastic strains. In Section 3, on the basis of this theory, we develop an inversion method to estimate 3-D elastic/inelastic strain fields from GPS data. In Section 4, we demonstrate the validity and availability of the inversion method through its application to GPS horizontal velocity data in the Niigata–Kobe transformation zone, central Japan.

## 2 THEORY OF PHYSICS-BASED STRAIN ANALYSIS WITH MOMENT TENSOR

In geodesy, so far, GPS array data have been analysed in a purely geometric way without considering the physical mechanism of crustal deformation, and so it has been impossible to estimate 3-D strain fields and divide them into elastic and inelastic parts. In geophysics, however, we have now a common understanding that the Earth's crust is a linear elastic body including a number of defects. The occurrence of inelastic deformation such as brittle fracture and/or plastic flow at the defects brings about elastic deformation in the surrounding regions. The crustal deformation observed through geodetic measurements is the sum of the inelastic deformation as source and the elastic deformation as effect. Taking such a physical mechanism of crustal deformation into consideration, we can create the theory of physics-based strain analysis to resolve a long-outstanding problem in geodesy: the separate estimation of 3-D elastic and inelastic strain.

### 2.1 Definition of moment tensor

We consider a solid body occupying the region  $V$  in a Cartesian coordinate system  $(x_1, x_2, x_3)$ , bounded by a surface  $\partial V$ . In the following discussion, we ignore the effects of self-gravitation and pre-stress, and use Einstein's summation convention for simplicity.

Then, the equilibrium equation of the solid body can be written as

$$\partial_j \sigma_{ij} + f_i = 0. \quad (1)$$

Here,  $\sigma_{ij}$  is actual physical stress,  $f_i$  is body force, and  $\partial_j$  denotes the partial derivative with respect to the coordinate  $x_j$ . Assuming the solid body to be linearly elastic, we can define model stress  $\tau_{ij}$  as

$$\tau_{ij} = c_{ijkl} \varepsilon_{kl}, \quad (2)$$

where  $\varepsilon_{kl}$  is Cauchy's infinitesimal strain tensor, and  $c_{ijkl}$  denotes the stiffness tensor of the concerned elastic body. Then, eq. (1) can be rewritten in terms of the model stress  $\tau_{ij}$  as

$$\partial_j \tau_{ij} + f_i + e_i = 0 \quad (3)$$

with

$$e_i = \partial_j \sigma_{ij} - \partial_j \tau_{ij}. \quad (4)$$

Here,  $e_i$  is a virtual force with the same dimension as the body force  $f_i$ . Following Backus & Mulcahy (1976a), we define moment density tensor  $m_{ij}$  as the difference of the model stress  $\tau_{ij}$  from the actual physical stress  $\sigma_{ij}$ :

$$m_{ij} = \tau_{ij} - \sigma_{ij}, \quad (5)$$

which is related with the virtual force  $e_i$  as

$$\partial_j m_{ij} = -e_i. \quad (6)$$

Now we divide the strain  $\varepsilon_{kl}$  into the elastic part  $\varepsilon_{kl}^e$  and the inelastic part  $\varepsilon_{kl}^a$ :

$$\varepsilon_{kl} = \varepsilon_{kl}^e + \varepsilon_{kl}^a. \quad (7)$$

Then, the physical stress  $\sigma_{ij}$  can be expressed as

$$\sigma_{ij} = c_{ijkl} \varepsilon_{kl}^e. \quad (8)$$

Substituting eqs (2) and (8) into eq. (5), we obtain

$$m_{ij} = c_{ijkl} (\varepsilon_{kl} - \varepsilon_{kl}^e) = c_{ijkl} \varepsilon_{kl}^a. \quad (9)$$

The above equation means that the product of the inelastic strain  $\varepsilon_{kl}^a$  multiplied by the stiffness tensor  $c_{ijkl}$  of the elastic body gives a moment density tensor  $m_{ij}$ , the spatial derivatives of which play a role of the virtual force that deforms surrounding elastic media in the equilibrium eq. (3) rewritten in terms of the model stress  $\tau_{ij}$ .

By the definition in eq. (5), we can represent any indigenous source in a linear elastic body with a moment tensor, which is the second-order symmetric tensor with diagonal elements of force dipoles and off-diagonal elements of force couples. Although the moment tensor is a mathematical concept introduced into linear elasticity theory to represent internal sources, it is directly related with physical substance, inelastic strain, by eq. (9). For instance, we can generally decompose a moment tensor into the three independent force systems corresponding to three basic deformation patterns; that is, isotropic expansion, crack opening and shear faulting. Such decomposition is natural and always possible by solving eigenvalue problems for a given moment tensor.

### 2.2 Representation of crustal deformation with moment tensor

Let the equilibrium state of the Earth's crust at a time  $t$  be written by eq. (3). We suppose that the inelastic strain  $\delta \varepsilon_{ij}^a(\mathbf{X})$  was generated by brittle fracture and/or plastic flow at the defects distributed in the Earth's crust for a time interval  $t \sim t + \delta t$ . Then, from eq. (9), the

corresponding moment density tensor distribution  $\delta m_{ij}(\mathbf{X})$  is given by

$$\delta m_{ij}(\mathbf{X}) = c_{ijkl} \delta \varepsilon_{kl}^a(\mathbf{X}). \quad (10)$$

Denoting static Green's tensor by  $G_{ip}(\mathbf{x}; \mathbf{X})$ , we can compute the displacement field  $u_i(\mathbf{x})$  caused by the moment density tensor distribution as

$$u_i(\mathbf{x}) = \int_V G_{ip,q}(\mathbf{x}; \mathbf{X}) \delta m_{pq}(\mathbf{X}) dV \quad (i = 1, 2, 3). \quad (11)$$

Here,  $G_{ip,q}(\mathbf{x}; \mathbf{X})$  represents the partial derivative of  $G_{ip}(\mathbf{x}; \mathbf{X})$  with respect to the source coordinate  $\xi_q$ . The explicit expressions of  $G_{ip,q}(\mathbf{x}; \mathbf{X})$  are given, for example, in Yabuki & Matsu'ura (1992) for an elastic half-space model and Hashima *et al.* (2008) for an elastic-viscoelastic layered model.

Differentiating both sides of eq. (11) with respect to the spatial coordinates  $x_j$ , we obtain the analytical expression of deformation gradient tensor  $\mathbf{D}$  with its  $ij$  element of  $\partial_j u_i$ . The symmetric part of the deformation gradient tensor,  $(\mathbf{D}^T + \mathbf{D})/2$ , gives the infinitesimal strain tensor  $\mathbf{E}$  with its  $ij$  element of

$$\varepsilon_{ij} = (\partial_j u_i + \partial_i u_j)/2, \quad (12)$$

but it is only the elastic part of strain tensor, because the spatial derivatives of displacements cannot be defined at source points in an analytical sense. To put it shortly, using analytical strain response functions  $H_{ijpq}(\mathbf{x}; \mathbf{X})$  to a unit moment tensor, we can compute the elastic strain field  $\delta \varepsilon_{ij}^e(\mathbf{x})$  caused by the moment density tensor distribution  $\delta m_{pq}(\mathbf{X})$  as

$$\delta \varepsilon_{ij}^e(\mathbf{x}) = \int_V H_{ijpq}(\mathbf{x}; \mathbf{X}) \delta m_{pq}(\mathbf{X}) dV \quad (i, j = 1, 2, 3). \quad (13)$$

By the way, moment density tensor is related with inelastic strain by eq. (9), and so the inelastic strain field  $\delta \varepsilon_{ij}^a(\mathbf{x})$  is directly obtained by converting the moment density tensor distribution  $\delta m_{pq}(\mathbf{x})$  with the compliance tensor  $s_{ijpq}$  of the elastic body as

$$\delta \varepsilon_{ij}^a(\mathbf{x}) = s_{ijpq} \delta m_{pq}(\mathbf{x}) \quad (i, j = 1, 2, 3). \quad (14)$$

As discussed in chapter 4 of Fung (1965) in detail, given the total strain, which is defined by the sum of the elastic strain and the inelastic strain as

$$\delta \varepsilon_{ij}(\mathbf{x}) = \delta \varepsilon_{ij}^e(\mathbf{x}) + \delta \varepsilon_{ij}^a(\mathbf{x}), \quad (15)$$

everywhere, we can correctly reproduce the displacement field in eq. (11). It should be noted that directly observable strain  $\varepsilon_{ij}^o(\mathbf{x})$  through geodetic measurements corresponds to the theoretical strain obtained by numerically differentiating the displacement field in eq. (11) with respect to spatial coordinates, which gives a smoothed total strain field. Therefore, as demonstrated by Haines (1982) and Haines & Holt (1993), we can reproduce the horizontal velocity fields from the observed strain-rate fields under some assumptions.

### 2.3 Intrinsic deformation extracted from GPS data

GPS is a system that determines the current coordinates  $\mathbf{x}$  of observation points in a geodetic reference frame (Hofmann-Wellenhof & Moritz 2005). The displacement data  $\mathbf{u}$  obtained by GPS measurements, which are the difference between the current and previous coordinates of observation points, contain not only intrinsic deformation but also rigid motion such as block translation and rotation. On the other hand, since the moment tensor is an internal force system with no net force and no net torque, the crustal deformation

caused by it is purely intrinsic one. Therefore, the theoretical displacements computed from eq. (11) should not be compared with GPS data directly but with the intrinsic deformation extracted from GPS data.

The deformation of continuum can be perfectly described by specifying the nine independent elements of deformation gradient tensor  $\mathbf{D} = [D_{ij}]$  defined by the spatial derivatives of the displacement vector  $\mathbf{u} = [u_i]$ . The symmetric part of the deformation gradient tensor,  $(\mathbf{D}^T + \mathbf{D})/2$ , gives the infinitesimal strain tensor  $\mathbf{E} = [\varepsilon_{ij}]$  and the antisymmetric part,  $(\mathbf{D}^T - \mathbf{D})/2$ , gives the infinitesimal rotation tensor  $\mathbf{\Omega} = [\omega_{ij}]$ . Here, it should be noted that the intrinsic deformation of continuum, which we want to know, is given by the strain tensor.

From GPS array data, unfortunately, we cannot obtain the vertical gradients of displacement vectors, because GPS measurements are restricted to the Earth's surface. Therefore, taking the  $x_3$ -axis vertically upwards, we can only determine horizontal strain ( $\varepsilon_{11}$ ,  $\varepsilon_{12}$ ,  $\varepsilon_{22}$ ) and horizontal rotation ( $\omega_{12}$ ). In the 2-D problem, from the definition of deformation gradient tensor, we can write the horizontal displacement field in the vicinity of a point  $\mathbf{x}$  as

$$\begin{cases} u_1(\mathbf{x} + d\mathbf{x}) = u_1(\mathbf{x}) + \varepsilon_{11}(\mathbf{x})dx_1 + \varepsilon_{12}(\mathbf{x})dx_2 - \omega_{12}(\mathbf{x})dx_2 \\ u_2(\mathbf{x} + d\mathbf{x}) = u_2(\mathbf{x}) + \varepsilon_{12}(\mathbf{x})dx_1 + \varepsilon_{22}(\mathbf{x})dx_2 + \omega_{12}(\mathbf{x})dx_1 \end{cases} \quad (16)$$

Given the displacement data at some observation points  $\mathbf{x} + d\mathbf{x}$  around the point  $\mathbf{x}$ , we can solve the above equations for  $u_1$ ,  $u_2$ ,  $\varepsilon_{11}$ ,  $\varepsilon_{12}$ ,  $\varepsilon_{22}$  and  $\omega_{12}$  by using a least-squares method. This is the basic idea of the geometric inversion method by Shen *et al.* (1996), which is the most orthodox way to estimate 2-D horizontal strain fields from GPS data under the assumption of locally uniform strain.

Now we rotate the coordinate system  $(x_1, x_2, x_3)$  around the vertical axis  $x_3$  so that the  $x_1$ -axis points to the direction of  $d\mathbf{x}$ . Then, in the new coordinate system  $(x'_1, x'_2, x_3)$ , eq. (16) can be rewritten as

$$\begin{cases} u'_1(\mathbf{x}' + d\mathbf{x}') - u'_1(\mathbf{x}') = \varepsilon'_{11}(\mathbf{x}')dx'_1 \\ u'_2(\mathbf{x}' + d\mathbf{x}') - u'_2(\mathbf{x}') = \varepsilon'_{12}(\mathbf{x}')dx'_1 + \omega'_{12}(\mathbf{x}')dx'_1 \end{cases} \quad (17)$$

From the above equations we can see that the  $x'_1$  component of the relative displacement vector gives simple extension in the new coordinate system. On the other hand, the  $x'_2$  component gives the inseparable composite of pure shear and rotation.

The rigid body translation and rotation contained in the observed GPS data cannot be explained by the theoretical model of moment density tensor. We can remove the rigid body translation by taking the difference between the displacement vectors at adjacent observation points, but not the rigid body rotation. If the data contain systematic errors (theoretically unexplainable coherent noise), the result of data analysis will be seriously biased. One of the ways to avoid this problem is to use only the baseline-length changes in eq. (17) as data. In fact, given the baseline-length change data, we can determine three horizontal strain components uniquely (e.g. Tsuboi 1932).

On the basis of such consideration, we extract the information about intrinsic deformation from GPS array data in the following way. First, we compose a triangle mesh from a set of observation points. Then, to eliminate the effects of rigid body translation and rotation, we transform observed displacement data  $\mathbf{u}_i^o = (u_i^o, v_i^o)$  and  $\mathbf{u}_j^o = (u_j^o, v_j^o)$  at two adjacent points  $P_i$  and  $P_j$  into baseline-length change data  $d_{ij}$  as

$$d_{ij} = \cos \theta_{ij} (u_j^o - u_i^o) + \sin \theta_{ij} (v_j^o - v_i^o), \quad (18)$$

where  $\theta_{ij}$  denotes the angle of the baseline  $P_i - P_j$  measured counter-clockwise from the  $x_1$ -axis. Rewriting eq. (18) for displacement components, we obtain

$$d_{ij} = \begin{bmatrix} -\cos\theta_{ij} & -\sin\theta_{ij} & \cos\theta_{ij} & \sin\theta_{ij} \end{bmatrix} \begin{bmatrix} u_i^o \\ v_i^o \\ u_j^o \\ v_j^o \end{bmatrix}. \quad (19)$$

Performing the same transformation for all the pairs of adjacent observation points, we can obtain a linear equation that define a data vector  $\mathbf{d}$  of baseline-length changes from a data vector  $\mathbf{u}^o$  of observed displacements as

$$\mathbf{d} = \mathbf{R}\mathbf{u}^o, \quad (20)$$

where  $\mathbf{R}$  is a transformation matrix, the elements of which are defined in eq. (19).

Since the baseline-length change data  $\mathbf{d}$  transformed from GPS displacement data  $\mathbf{u}^o$  by eq. (20) have the information about intrinsic crustal deformation only, we can now directly compare them with the theoretical displacements  $\mathbf{u}$  computed from eq. (11) after the transformation with the same matrix  $\mathbf{R}$  in eq. (20) as

$$\Delta\mathbf{u} = \mathbf{R}\mathbf{u}. \quad (21)$$

Here,  $\Delta\mathbf{u}$  represents a theoretical baseline-length change vector. Thus, putting eqs (11), (20) and (21) together, we can relate the moment density tensor distribution  $\delta m_{ij}(\boldsymbol{\xi})$  to the observed baseline-length change data  $\mathbf{d}$  quantitatively, and so define the inverse problem of estimating the moment density tensor distribution from observed GPS data. Solving the inverse problem, we can obtain the optimum moment density tensor distribution  $\delta \hat{m}_{ij}(\boldsymbol{\xi})$ . Given the optimum moment density tensor distribution, we can directly obtain the inelastic strain field  $\delta \varepsilon_{ij}^o(\mathbf{x})$  by using eq. (14) and theoretically compute the elastic strain field  $\delta \varepsilon_{ij}^e(\mathbf{x})$  by using eq. (13).

### 3 MATHEMATICAL FORMULATION OF THE INVERSE PROBLEM

On the theory of physics-based strain analysis, we mathematically formulate the inversion method to separately estimate 3-D elastic and inelastic strain fields from GPS array data. In this method, first, the optimum distribution of moment density tensor in the Earth's crust is determined by using Akaike's information criterion (AIC) (Akaike 1974). Then, the elastic and inelastic strain fields are obtained from the optimum moment density tensor distribution by theoretical computation and direct conversion with elastic compliance tensor, respectively.

#### 3.1 Observation equations

We take a Cartesian coordinate system  $(x, y, z)$  so that the  $x$ - $y$  plane coincides with the Earth's surface and the  $z$ -axis points vertically upwards, and define a box-type model region  $V$ . To discretize the problem, we represent the spatial distribution of each element of moment density tensor  $\delta m_{pq}(x, y, z)$  in the model region by the superposition of a finite number ( $R$ ) of known 3-D basis functions  $\Phi_r(x, y, z)$  defined in  $V$  as

$$\delta m_{pq}(x, y, z) = \sum_{r=1}^R a_r^{pq} \Phi_r(x, y, z). \quad (22)$$

Substituting the above expression into eq. (11), we can represent the horizontal displacement components  $u_i$  ( $i = x, y$ ) at a point  $\mathbf{x}_j = (x_j, y_j, 0)$  on the Earth's surface due to the moment density tensor distribution as a linear combination of the expansion coefficients  $a_r^{pq}$ :

$$u_i(\mathbf{x}_j) = \sum_{p=1}^3 \sum_{q=p}^3 \sum_{r=1}^R G_{ir}^{pq}(\mathbf{x}_j) a_r^{pq} \quad (23)$$

with

$$G_{ir}^{pq}(\mathbf{x}_j) = \int_V \bar{G}_{ip,q}(x_j, y_j, 0; x', y', z') \Phi_r(x', y', z') dx' dy' dz'. \quad (24)$$

Here, because of the symmetry of moment tensor, we used  $\bar{G}_{ip,q}$ , defined by the following equation, instead of  $G_{ip,q}$ :

$$\begin{cases} \bar{G}_{ip,q} = G_{ip,q} & \text{for } q = p \\ \bar{G}_{ip,q} = (G_{ip,q} + G_{iq,p}) & \text{for } q > p \end{cases}. \quad (25)$$

Thus, denoting the surface displacement vector by  $\mathbf{u}$ , the model parameter vector by  $\mathbf{a}$ , and the coefficient matrix that connects them by  $\mathbf{G}$ , we can rewrite eq. (23) in vector form as

$$\mathbf{u} = \mathbf{G}\mathbf{a}. \quad (26)$$

The dimensions of  $\mathbf{u}$ ,  $\mathbf{a}$  and  $\mathbf{G}$  are  $2N \times 1$  ( $N$  is the number of observation points),  $6R \times 1$  ( $R$  is the number of basis functions) and  $2N \times 6R$ , respectively.

From eqs (20), (21) and (26), we finally obtain a set of linear observation equations to be solved for the model parameter  $\mathbf{a}$ :

$$\mathbf{d} = \mathbf{H}\mathbf{a} + \mathbf{e}, \quad \mathbf{e} \sim N(\mathbf{0}, \sigma^2 \mathbf{F}) \quad (27)$$

with

$$\mathbf{H} = \mathbf{R}\mathbf{G}. \quad (28)$$

Here,  $\mathbf{d}$  is an  $n$ -dimensional data vector ( $n$  is the number of baselines),  $\mathbf{a}$  is an  $m$ -dimensional model parameter vector ( $m$  is the product of the number of basis functions  $R$  multiplied by 6),  $\mathbf{H}$  is an  $n \times m$  dimensional coefficient matrix, and  $\mathbf{e}$  is an  $n$ -dimensional data error vector. The Gaussian data errors  $\mathbf{e}$  in eq. (27) generally consist of observation errors in GPS measurements and modelling errors due to imperfection in theoretical representation of crustal deformation, and so we may suppose that the covariance matrix  $\mathbf{F}$  takes the form of

$$\mathbf{F} = \mathbf{R}\mathbf{E}\mathbf{R}^T + c^2 \mathbf{D} \quad (29)$$

with

$$E_{ij} = \left(1 + b^2 |u_i^o / \bar{u}^o|^2\right) \delta_{ij}, \quad (30)$$

$$D_{ij} = |l_i / \bar{l}|^2 \delta_{ij}. \quad (31)$$

Here,  $|u_i^o / \bar{u}^o|$  in eq. (30) is the relative magnitude of the  $i$ th displacement component  $u_i^o$  to a standard value  $\bar{u}^o$ ,  $|l_i / \bar{l}|$  in eq. (31) is the relative value of the  $i$ th baseline length  $l_i$  to a standard baseline length  $\bar{l}$ , and  $b^2$  and  $c^2$  are some weighting constants.

#### 3.2 Generalized inverse matrix and the optimum solution

We use Lanczos' singular value decomposition (SVD) technique of a rectangular matrix (Lanczos 1961) to solve the observation equation and AIC based on the entropy maximization principle (Akaike 1977) to select the optimum solution. First, we normalize

the observation eq. (27) so that the covariance matrix  $\mathbf{F}$  becomes a unit matrix  $\mathbf{I}$ . The normalization is done in the following procedure. (1) Decompose the covariance matrix  $\mathbf{F}$  into the product of an  $n \times n$  diagonal matrix  $\mathbf{\Sigma}$  composed of the  $n$  positive eigenvalues of  $\mathbf{F}$ , an  $n \times n$  matrix  $\mathbf{W}$  composed of the corresponding eigenvectors and its transpose  $\mathbf{W}^T$  as

$$\mathbf{F} = \mathbf{W}\mathbf{\Sigma}\mathbf{W}^T. \quad (32)$$

(2) Define an  $n \times n$  matrix  $\mathbf{T}$  as

$$\mathbf{T} = \mathbf{\Sigma}^{-1/2}\mathbf{W}^T, \quad (33)$$

where  $\mathbf{\Sigma}^{-1/2}$  is a diagonal matrix with its non-zero elements of the inverse of the square roots of the eigenvalues. (3) Transform the data vector  $\mathbf{d}$ , error vector  $\mathbf{e}$  and coefficient matrix  $\mathbf{H}$  in the observation eq. (27) by  $\mathbf{T}$  as

$$\mathbf{d}' = \mathbf{T}\mathbf{d}, \quad \mathbf{e}' = \mathbf{T}\mathbf{e} \quad \text{and} \quad \mathbf{H}' = \mathbf{T}\mathbf{H}. \quad (34)$$

Thus, we obtain the normalized observation equation with the associated covariance matrix  $\mathbf{F}' = \mathbf{T}\mathbf{F}\mathbf{T}^T = \mathbf{I}$  of the data errors  $\mathbf{d}'$ :

$$\mathbf{d}' = \mathbf{H}'\mathbf{a} + \mathbf{e}', \quad \mathbf{e}' \sim N(\mathbf{0}, \sigma^2\mathbf{I}). \quad (35)$$

Next, following Lanczos (1961), we decompose the coefficient matrix  $\mathbf{H}'$  of the normalized observation equation as

$$\mathbf{H}' = \mathbf{U}_p\mathbf{\Lambda}_p\mathbf{V}_p^T \quad p \leq \min(n, m), \quad (36)$$

where  $\mathbf{\Lambda}_p$  is a  $p \times p$  diagonal matrix composed of the  $p$  positive eigenvalues of  $\mathbf{H}'$ ,  $\mathbf{U}_p$  is an  $n \times p$  semi-orthonormal matrix composed of the corresponding eigenvectors in data space, and  $\mathbf{V}_p^T$  is the transpose of an  $m \times p$  semi-orthonormal matrix composed of the corresponding eigenvectors in model parameter space. Then, Lanczos' generalized inverse matrix  $\mathbf{H}'^\dagger$  is defined as

$$\mathbf{H}'^\dagger = \mathbf{V}_p\mathbf{\Lambda}_p^{-1}\mathbf{U}_p^T. \quad (37)$$

The solution of eq. (35) by the Lanczos' generalized inverse matrix,

$$\hat{\mathbf{a}} = \mathbf{H}'^\dagger\mathbf{d}' = \mathbf{V}_p\mathbf{\Lambda}_p^{-1}\mathbf{U}_p^T\mathbf{d}', \quad (38)$$

gives a unique solution that minimizes the square norm of the residual vector,

$$\|\mathbf{d}' - \mathbf{H}'\hat{\mathbf{a}}\|_2^2 = (\mathbf{d}' - \mathbf{H}'\hat{\mathbf{a}})^T\mathbf{F}'^{-1}(\mathbf{d}' - \mathbf{H}'\hat{\mathbf{a}}), \quad (39)$$

and the square norm of the solution vector,  $\|\hat{\mathbf{a}}\|_2^2$ , simultaneously.

Now we consider the stochastic model and maximum likelihood solution for the same problem. From the observation eq. (27), we obtain the corresponding probability density function as

$$p(\mathbf{d}|\mathbf{a}; \sigma^2) = (2\pi\sigma^2)^{-n/2} \|\mathbf{F}\|^{-1/2} \exp\left[-\frac{1}{2\sigma^2}s(\mathbf{a})\right] \quad (40)$$

with

$$s(\mathbf{a}) = (\mathbf{d} - \mathbf{H}\mathbf{a})^T\mathbf{F}^{-1}(\mathbf{d} - \mathbf{H}\mathbf{a}). \quad (41)$$

Then, the log likelihood of the stochastic model is given by

$$\log l(\mathbf{a}; \sigma^2|\mathbf{d}) = -\frac{n}{2} \log 2\pi\sigma^2 - \frac{1}{2} \log \|\mathbf{F}\| - \frac{1}{2\sigma^2}s(\mathbf{a}). \quad (42)$$

From the necessary conditions for maximizing the log likelihood,

$$\partial \log l(\mathbf{a}; \sigma^2|\mathbf{d})/\partial \mathbf{a} = 0 \quad \text{and} \quad \partial \log l(\mathbf{a}; \sigma^2|\mathbf{d})/\partial \sigma^2 = 0, \quad (43)$$

we obtain the maximum likelihood estimates of  $\mathbf{a}$  and  $\sigma^2$  as

$$\hat{\mathbf{a}} = (\mathbf{H}^T\mathbf{F}^{-1}\mathbf{H})^{-1}\mathbf{H}^T\mathbf{F}^{-1}\mathbf{d}, \quad (44)$$

$$\hat{\sigma}^2 = s(\hat{\mathbf{a}})/n. \quad (45)$$

Here, it should be noted that the maximum likelihood solution in eq. (44) is mathematically equivalent to the generalized least-squares solution in eq. (38). Using the relation  $\mathbf{T}\mathbf{F}\mathbf{T}^T = \mathbf{I}$ , we can prove it as follows:

$$\begin{aligned} (\mathbf{H}'^T\mathbf{F}'^{-1}\mathbf{H}')^{-1}\mathbf{H}'^T\mathbf{F}'^{-1}\mathbf{d}' &= [(\mathbf{T}\mathbf{H})^T(\mathbf{T}\mathbf{H})]^{-1}(\mathbf{T}\mathbf{H})^T(\mathbf{T}\mathbf{d}) \\ &= [\mathbf{H}'^T\mathbf{H}']^{-1}\mathbf{H}'^T\mathbf{d}' = [\mathbf{V}_p\mathbf{\Lambda}_p^2\mathbf{V}_p^T]^{-1}\mathbf{V}_p\mathbf{\Lambda}_p\mathbf{U}_p^T\mathbf{d}' \\ &= \mathbf{V}_p\mathbf{\Lambda}_p^{-1}\mathbf{U}_p^T\mathbf{d}' = \mathbf{H}'^\dagger\mathbf{d}'. \end{aligned} \quad (46)$$

The covariance matrix of estimation errors for the generalized least-squares solution in (38), and so that for the maximum likelihood solution in eq. (44), is evaluated as

$$\begin{aligned} \mathbf{C}(\hat{\mathbf{a}}) &= (\mathbf{H}'^\dagger)(\hat{\sigma}^2\mathbf{I})(\mathbf{H}'^\dagger)^T = \hat{\sigma}^2(\mathbf{V}_p\mathbf{\Lambda}_p^{-1}\mathbf{U}_p^T)(\mathbf{V}_p\mathbf{\Lambda}_p^{-1}\mathbf{U}_p^T)^T \\ &= \hat{\sigma}^2\mathbf{V}_p\mathbf{\Lambda}_p^{-2}\mathbf{V}_p^T. \end{aligned} \quad (47)$$

Then, the variance of estimation errors for the  $j$ th model parameter is given by

$$\text{var}(\hat{a}_j) \equiv [\mathbf{C}(\hat{\mathbf{a}})]_{jj} = \hat{\sigma}^2 \sum_{k=1}^p (V_{jk}/\lambda_k)^2 \quad (j = 1, \dots, m). \quad (48)$$

This equation means that the estimation errors of the generalized least-squares solution diverge if the smallest positive eigenvalue  $\lambda_p$  of the coefficient matrix  $\mathbf{H}'$  approaches to zero. To avoid such difficulty, Jackson (1972) and Wiggins (1972) have proposed a practical method called 'sharp cut-off approach'. In this approach we construct a linear inverse operator  $\mathbf{H}'_q^\dagger$  from the diagonal matrix,  $\mathbf{\Lambda}_q$ , composed of  $q$  ( $\leq p$ ) largest positive eigenvalues and the semi-orthonormal matrices,  $\mathbf{U}_q$  and  $\mathbf{V}_q$ , composed of the corresponding eigenvectors as

$$\mathbf{H}'_q^\dagger = \mathbf{V}_q\mathbf{\Lambda}_q^{-1}\mathbf{U}_q^T, \quad (49)$$

so that the variance of estimation errors for each model parameter becomes smaller than a given maximum allowable variance.

The solution obtained by the sharp cut-off of the sequence of positive eigenvalues,

$$\hat{\mathbf{a}}_q = \mathbf{H}'_q^\dagger\mathbf{d}' = \mathbf{V}_q\mathbf{\Lambda}_q^{-1}\mathbf{U}_q^T\mathbf{d}', \quad (50)$$

is no longer the generalized least-squares solution or the maximum likelihood solution in the original  $m$ -dimensional model parameter space. However, it can be regarded as the maximum likelihood solution in the  $q$ -dimensional subspace of the new model parameter space transformed from the original model parameter space with the semi-orthonormal matrix  $\mathbf{V}_p = [\mathbf{v}_1, \dots, \mathbf{v}_p]$ . Therefore, to select the optimum solution from among the maximum likelihood solutions  $\hat{\mathbf{a}}_q$  with different degrees of freedom  $q$ , we can use AIC defined by

$$\text{AIC}(q) = -2 \log l(\hat{\mathbf{a}}_q; \hat{\sigma}_q^2|\mathbf{d}) + 2q, \quad (51)$$

where

$$\log l(\hat{\mathbf{a}}_q; \hat{\sigma}_q^2|\mathbf{d}) = -\frac{n}{2} \log 2\pi\hat{\sigma}_q^2 - \frac{1}{2} \log \|\mathbf{F}\| - \frac{n}{2} \quad (52)$$

with

$$\hat{\sigma}_q^2 = s(\hat{\mathbf{a}}_q)/n, \quad (53)$$

$$s(\hat{\mathbf{a}}_q) = (\mathbf{d}' - \mathbf{H}'\hat{\mathbf{a}}_q)^T(\mathbf{d}' - \mathbf{H}'\hat{\mathbf{a}}_q) = (\mathbf{d} - \mathbf{H}\hat{\mathbf{a}}_q)^T\mathbf{F}^{-1}(\mathbf{d} - \mathbf{H}\hat{\mathbf{a}}_q). \quad (54)$$

Thus, we finally obtain the criterion to select the optimum model:

$$\text{AIC}(q) = n \log \|\mathbf{d}' - \mathbf{H}'\hat{\mathbf{a}}_q\|_2^2 + 2q + C. \quad (55)$$

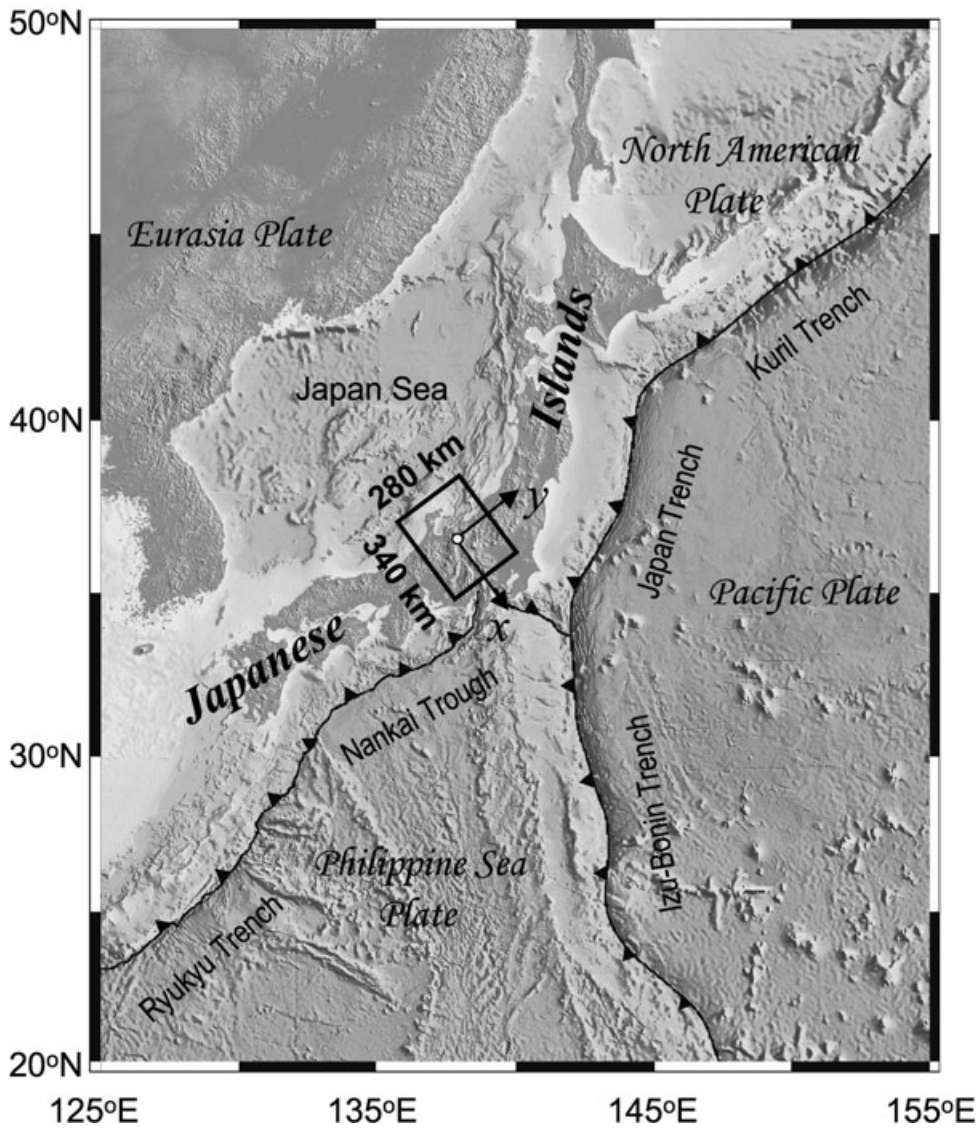


**Figure 1.** The model region, coordinate system and tectonic setting in and around Japan. The solid rectangle indicates the model region in this analysis. The origin of Cartesian coordinates  $(x, y, z)$  is taken at the centre  $(36.7^\circ\text{N}, 137.9^\circ\text{E})$  of the model region. The  $z$ -axis is taken to be vertically upwards.

#### 4 APPLICATION TO GPS VELOCITY DATA IN CENTRAL JAPAN

We apply the inversion method developed in Section 3 to GPS horizontal velocity data in the northern part of central Japan to estimate the 3-D distribution of elastic and inelastic strain rates there. As the model region of inversion analysis, we take a  $340\text{ km} \times 280\text{ km}$  rectangular region with the depth range of  $0\text{--}40\text{ km}$ , including the Niigata–Kobe transformation zone. The model region and coordinate system are shown in Fig. 1 together with tectonic setting in and around Japan. In modelling, we ignored fault-slip excess or deficit at plate interfaces, because its direct effect on crustal deformation in the northern part of central Japan is negligible (Sagiya *et al.* 2000; Hashimoto *et al.* 2004).

##### 4.1 Expressions of basis functions

We take the origin of Cartesian coordinates  $(x, y, z)$  at the centre of the rectangular region  $(36.7^\circ\text{N}, 137.9^\circ\text{E})$ . Then, the box-type model

region  $V$  is defined as

$$\begin{cases} -X \leq x \leq X \\ -Y \leq y \leq Y \\ -Z \leq z \leq 0 \end{cases} \quad (56)$$

with

$$X = 170, \quad Y = 140 \quad \text{and} \quad Z = 40\text{ km}. \quad (57)$$

Normalizing the coordinates  $x, y$  and  $z$  by  $X, Y$  and  $Z$ , respectively, as

$$\xi = x/X, \quad \eta = y/Y \quad \text{and} \quad \zeta = z/Z, \quad (58)$$

we transform the model region defined in eq. (56) into

$$\begin{cases} -1 \leq \xi \leq 1 \\ -1 \leq \eta \leq 1 \\ -1 \leq \zeta \leq 0 \end{cases} . \quad (59)$$

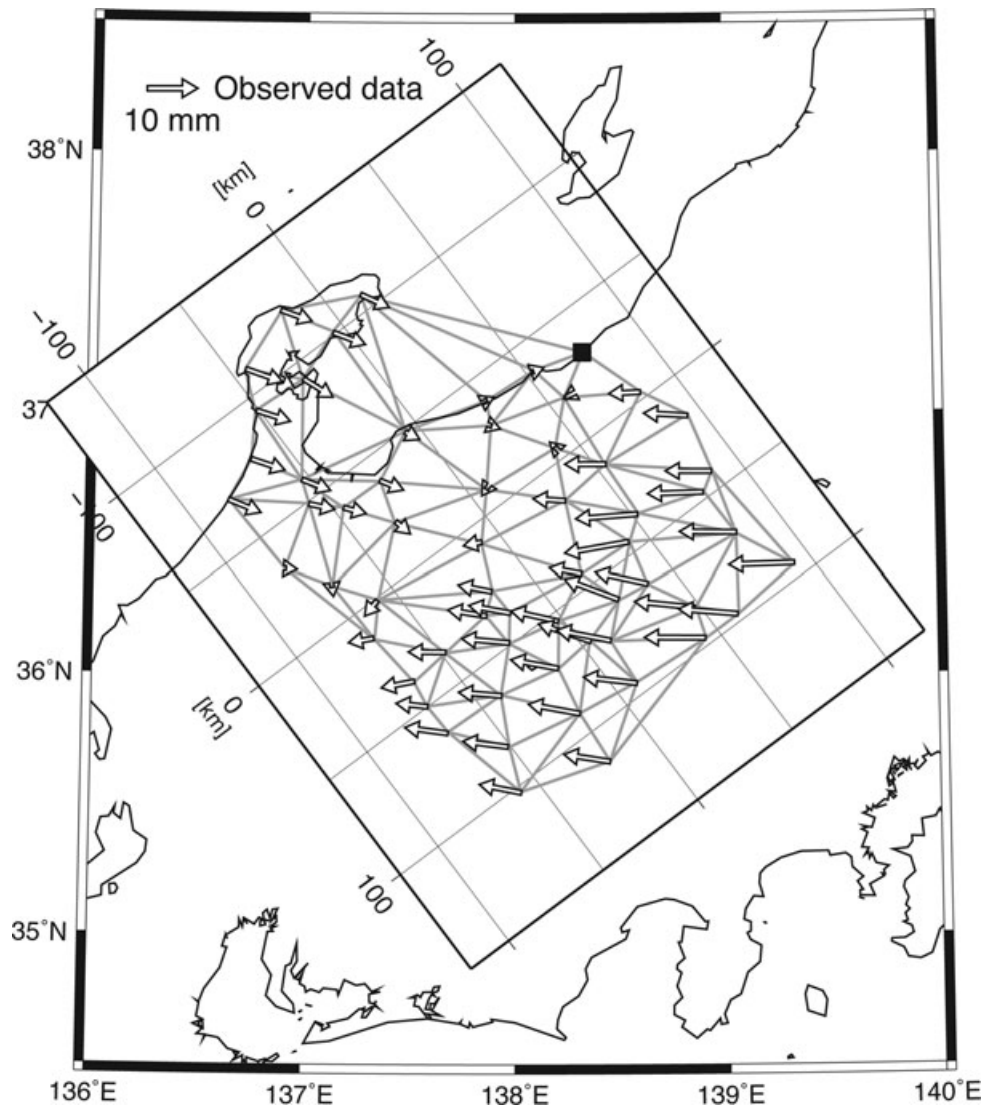


**Figure 2.** The GPS horizontal velocity data used for inversion analysis. The open arrows indicate observed horizontal velocity vectors at 60 GPS stations, which represent relative velocities to the fixed point denoted by a closed square. The grey solid lines are the baselines of the optimum triangle mesh composed of the GPS stations with Delaunay triangulation.

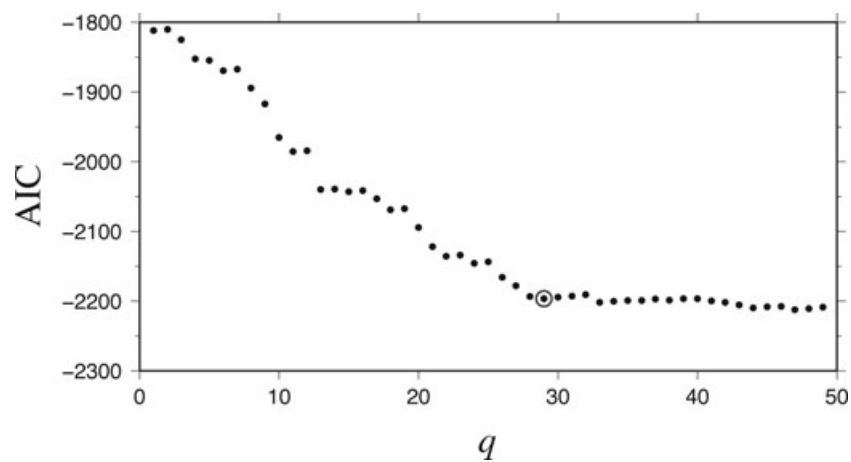


**Figure 3.** The values of AIC plotted as a function of the degree of freedom  $q$  of the model. The open circle indicates the optimum number of  $q$  ( $= 29$ ), at which AIC takes a local minimum.

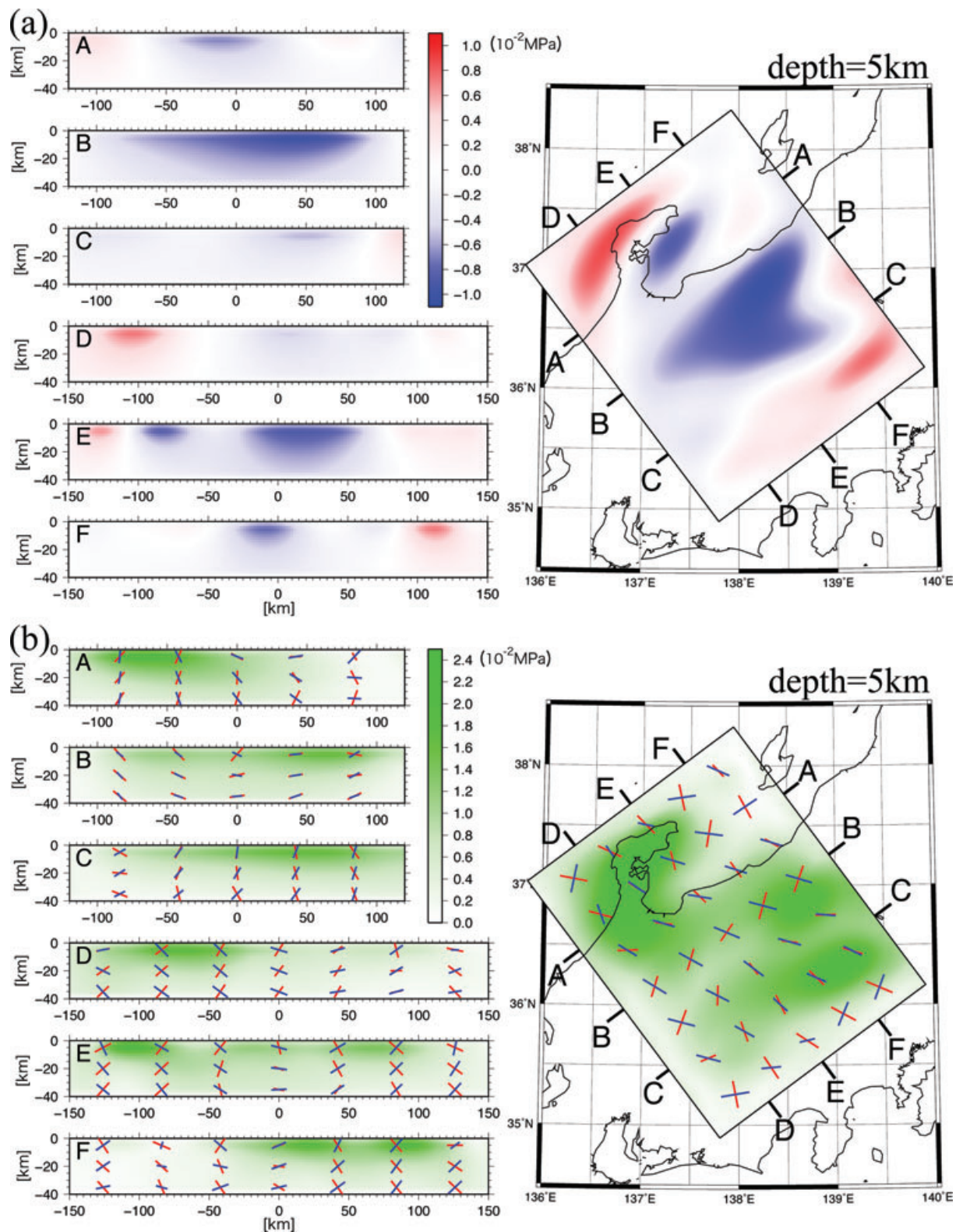


**Figure 4.** The moment rate density tensor distribution inverted from GPS horizontal velocity data. (a) Isotopic part. The red and blue of the colour-bar scale indicate expansion and compression, respectively. (b) Deviatoric part. The colour-bar scale represents the magnitude of maximum shear. The red and blue bars indicate the directions of maximum tension and compression, respectively. In each diagram, the right-hand panel shows the horizontal section at the depth of 5 km and the left-hand panels show the vertical sections along the lines A ~ F.



We represent the 3-D basis functions  $\Phi_r(\xi, \eta, \zeta)$  defined in the normalized model region as the product of three basis functions:

$$\Phi_{r(k,l,m)}(\xi, \eta, \zeta) = T_k(\xi)T_l(\eta)L_m(\zeta) \quad (60)$$

with

$$\begin{cases} T_k(\xi): & -1 \leq \xi \leq 1, & k = 0, \dots, K \\ T_l(\eta): & -1 \leq \eta \leq 1, & l = 0, \dots, L \\ L_m(\zeta): & -1 \leq \zeta \leq 0, & m = 0, \dots, M \end{cases} \quad (61)$$

As the basis functions  $T_k(\xi)$  and  $T_l(\eta)$ , we take the normalized Chebyshev polynomials, defined by

$$T_n(\chi) = \begin{cases} \sqrt{\frac{1}{\pi}} \frac{C_n(\chi)}{\sqrt{1-\chi^2}} & (n=0) \\ \sqrt{\frac{2}{\pi}} \frac{C_n(\chi)}{\sqrt{1-\chi^2}} & (n \neq 0) \end{cases} \quad (62)$$

The Chebyshev polynomials  $C_n(\chi)$  have the following orthogonality:

$$\int_{-1}^1 \frac{C_n(\chi)C_m(\chi)}{\sqrt{1-\chi^2}} d\chi = \begin{cases} 0 & (m \neq n) \\ \pi/2 & (m = n \neq 0) \\ \pi & (m = n = 0) \end{cases} \quad (63)$$

and so the basis functions  $T_n(\chi)$  are orthonormal:

$$\int_{-1}^1 T_n(\chi)T_m(\chi)d\chi = \delta_{nm}. \quad (64)$$

Although the basis function  $T_n(\chi)$  diverges at the edges of the model region ( $\chi = \pm 1$ ), it keeps good properties of the Chebyshev polynomials except the edges. As the basis functions  $L_m(\zeta)$ , on the

other hand, we take the first-order splines defined by

$$L_0(\zeta) = (1 + \zeta/\Delta s)[H(\zeta + \Delta s) - H(\zeta)] \quad \text{for } -\Delta s \leq \zeta \leq 0 \quad (65)$$

$$\begin{aligned} L_m(\zeta) = & ((m+1) + \zeta/\Delta s)[H(\zeta + (m+1)\Delta s) - H(\zeta + m\Delta s)] \\ & - ((m-1) + \zeta/\Delta s)[H(\zeta + m\Delta s) - H(\zeta + (m-1)\Delta s)] \\ & \text{for } -(m+1)\Delta s \leq \zeta \leq -(m-1)\Delta s \quad (m = 1, \dots, 7) \end{aligned} \quad (66)$$

with

$$\Delta s = 5/40 = 0.125. \quad (67)$$

Here,  $L_m$  ( $m = 1, \dots, 7$ ) are full first-order splines,  $L_0$  is a half first-order spline with its peak at the surface, and  $H(\zeta)$  denotes the Heaviside step function.

Substituting the above expressions of basis functions into eq. (22), we obtain the moment density tensor distribution in the actual model space as

$$\delta m_{pq}(x, y, z) = \sum_{k=0}^K \sum_{l=0}^L \sum_{m=0}^M a_{klm}^{pq} T_k\left(\frac{x}{X}\right) T_l\left(\frac{y}{Y}\right) L_m\left(\frac{z}{Z}\right). \quad (68)$$

Then, the expressions of surface displacements in eq. (23) can be rewritten as

$$u_i(\mathbf{x}_j) = \sum_{p=1}^3 \sum_{q=p}^3 \sum_{k=0}^K \sum_{l=0}^L \sum_{m=0}^M G_{iklm}^{pq}(\mathbf{x}_j) a_{klm}^{pq} \quad (69)$$

with

$$\begin{aligned} G_{iklm}^{pq}(\mathbf{x}_j) = & \int_V \tilde{G}_{ip,q}(x_j, y_j, 0; x', y', z') \\ & \times T_k\left(\frac{x'}{X}\right) T_l\left(\frac{y'}{Y}\right) L_m\left(\frac{z'}{Z}\right) dx' dy' dz'. \end{aligned} \quad (70)$$

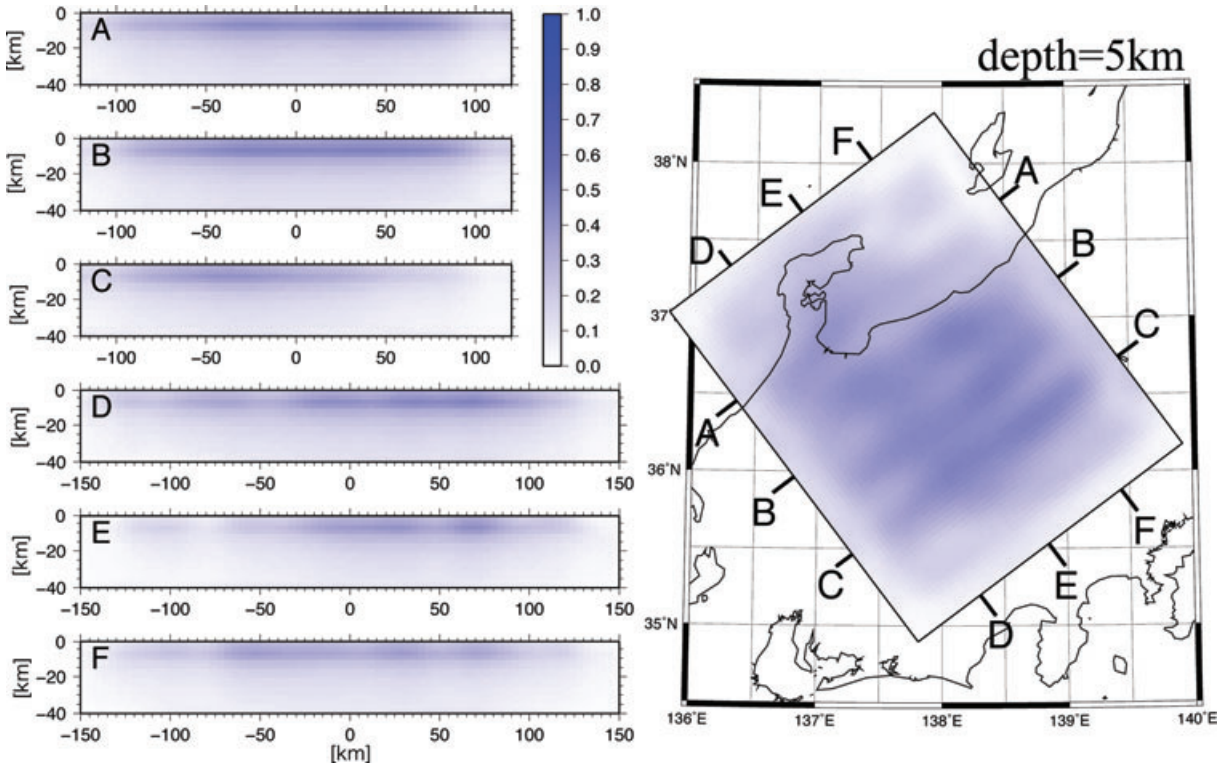


**Figure 5.** The resolution of the inverted moment rate density tensor distribution. The colour gradation contours represent the resolution of the isotropic part in Fig. 4(a). The right-hand panel shows the horizontal section at the depth of 5 km, and the left-hand panels show the vertical sections along the lines A ~ F.

#### 4.2 Data and data errors

To monitor the crustal movements of Japanese Islands, a nationwide dense GPS network (GEONET) has been operated by Geographical Survey Institute of Japan since 1996. From GPS daily coordinate data, Sagiya (2004) has obtained horizontal displacement rates (velocities) at GEONET stations for the interseismic calm period of 1996–2000 with the same least-squares collocation method as in Sagiya *et al.* (2000). In this inversion analysis, we used the horizontal velocity data at 60 GPS stations in Fig. 2, which are considered to be unaffected by fault-slip excess or deficit at plate interfaces. Here, the open arrows represent the horizontal velocities relative to the fixed point denoted by a closed square, and the grey solid lines are the baselines of the optimum triangle mesh composed of the GPS stations with the method of Delaunay triangulation (e.g. De Berg *et al.* 1997). The Delaunay triangulation method is necessary for constructing the optimum triangle mesh that minimizes estimation errors in strain analysis. Using the matrix  $\mathbf{R}$  defined in Section 2.3, we transformed the 60 horizontal velocity data into 157 baseline-length change rate data.

From Fig. 2 we can see that the spatial variation of velocity vectors in the  $x$ -direction is much greater than that in the  $y$ -direction, and so

we took the highest orders  $K$  and  $L$  of basis functions (normalized Chebyshev polynomials) in the  $x$ - and  $y$ -directions to be 15 and 6, respectively. On the other hand, we took the number  $M$  of basis functions (first-order splines) in the  $z$ -directions to be 7 to cover the depth range of 0–40 km. Then, the total number of unknown model parameters is  $6 \times (15 + 1) \times (6 + 1) \times (7 + 1) = 5376$ . Since the number of observed data is only 157, the observation eq. (27) is highly ill-conditioned.

To completely describe the problem, we need to compute the coefficient matrix  $\mathbf{H}$  in eq. (27) or  $\mathbf{G}$  in eq. (26) and specify the covariance matrix  $\mathbf{F}$  of data errors. In this local-scale analysis, we may ignore the effects of viscoelastic deformation in the asthenosphere underlying the 40-km-thick elastic model region; because the surface deformation originated in the asthenosphere has a much longer wavelength and much smaller amplitude than that originated in the crust. So we computed the coefficient matrix  $\mathbf{G}$  from eq. (70) by using the analytical expressions of surface displacements for a moment tensor source in elastic half-space (Yabuki & Matsu'ura 1992). As for the covariance matrix  $\mathbf{F}$ , we took the values of the standard velocity  $\bar{u}^o$  and the weighting constant  $b^2$  in eq. (30) to be  $10 \text{ mm yr}^{-1}$  and  $1 \times 10^{-1}$ , respectively, and the values of the standard baseline length  $\bar{l}$  in eq. (31) and the weighting constant  $c^2$  in eq.

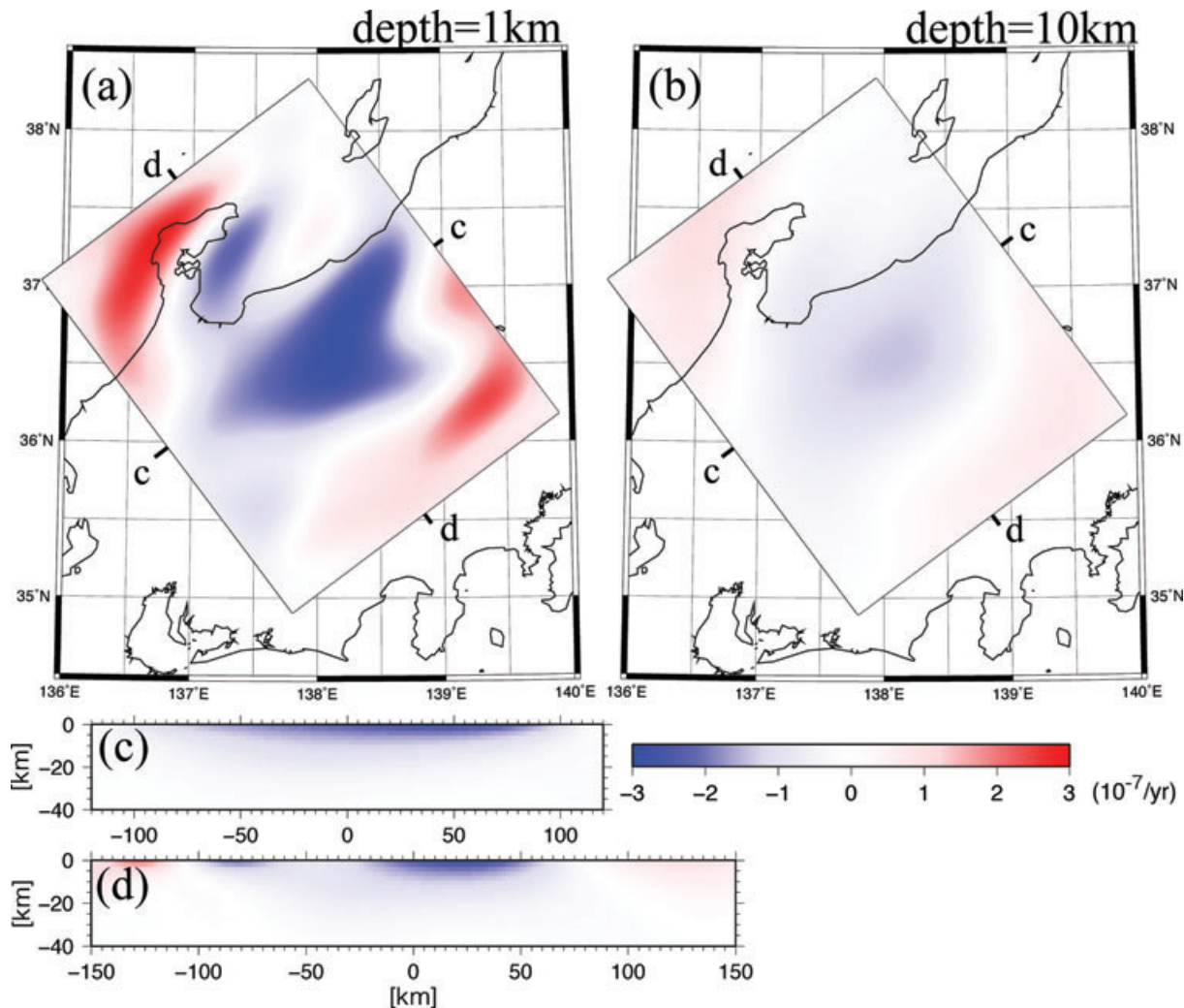


**Figure 6.** The total dilatation rates computed from the optimum moment rate density tensor distribution. The panels (a) and (b) show the horizontal sections at the depths of 1 km and 10 km, respectively. The panels (c) and (d) show the vertical sections along the lines c and d, respectively. The red and blue of the colour-bar scale indicate dilatation and contraction, respectively.

(29) to be 20 km and  $2 \times 10^{-1}$ , respectively. The standard deviation (measurement error) of each horizontal velocity component, which has been obtained from the daily coordinates of GPS stations for 1996–2000 with the least-squares collocation method, is about 2 mm  $\text{yr}^{-1}$  on average (table S1 of Hashimoto *et al.* 2009). So, the above setting of  $\bar{u}^o$ ,  $b^2$ ,  $\bar{l}$  and  $c^2$  means that the modelling errors (mm  $\text{yr}^{-1}$ ) for surface displacement rates and baseline-length change rates are assumed to be proportional to their magnitudes in mm  $\text{yr}^{-1}$  with the constant of 0.04 and their baseline-lengths in km with the constant of 0.03, respectively.

### 4.3 Inverted strain fields

Following the procedure described in Section 3.2, we inverted the baseline-length change rate data. In Fig. 3 we plotted the values of AIC as a function of  $q$  (the degree of freedom of the model). The AIC rapidly decreases up to  $q = 29$ , and then gradually increases up to  $q = 40$  with a small offset at  $q = 33$ . The gradual AIC decrease beyond  $q = 40$  is insignificant, because AIC loses its validity when the degree of freedom  $q$  becomes much larger than  $2\sqrt{n}$  (twice the square root of the number of data). On the other hand, the

irregular variation of AIC, including the small offset at  $q = 33$ , probably comes from some systematic errors due to imperfection in modelling. Actually, the test analysis of synthetic data with random errors shows the rather smooth variation of AIC with a clear global minimum. From these considerations, we adopted  $q = 29$  as the optimum degree of freedom of the model. Given the optimum degree of freedom, we can compute the optimum moment rate density tensor distribution  $\dot{m}_{pq}(x, y, z) = \delta m_{pq}(x, y, z)/\delta t$  from eqs (50) and (68).

The inverted moment rate density tensor distribution is shown in Fig. 4. For convenience in visual representation, we separate the inverted moment rate density tensor into the isotropic and deviatoric parts, which correspond to the dilatation and maximum shear strain rates, respectively. Fig. 4(a) shows the horizontal distribution of the isotropic part of moment rate density tensor at the depth of 5 km (right-hand side) and the vertical distributions along the six lines A ~ F (left-hand side). From this figure we can see that a remarkable compressional source region spreads in the central part. Fig. 4(b) shows the horizontal distribution of the deviatoric part of moment rate density tensor at the depth of 5 km (right-hand side) and the vertical distributions along the six lines A ~ F (left-hand side)

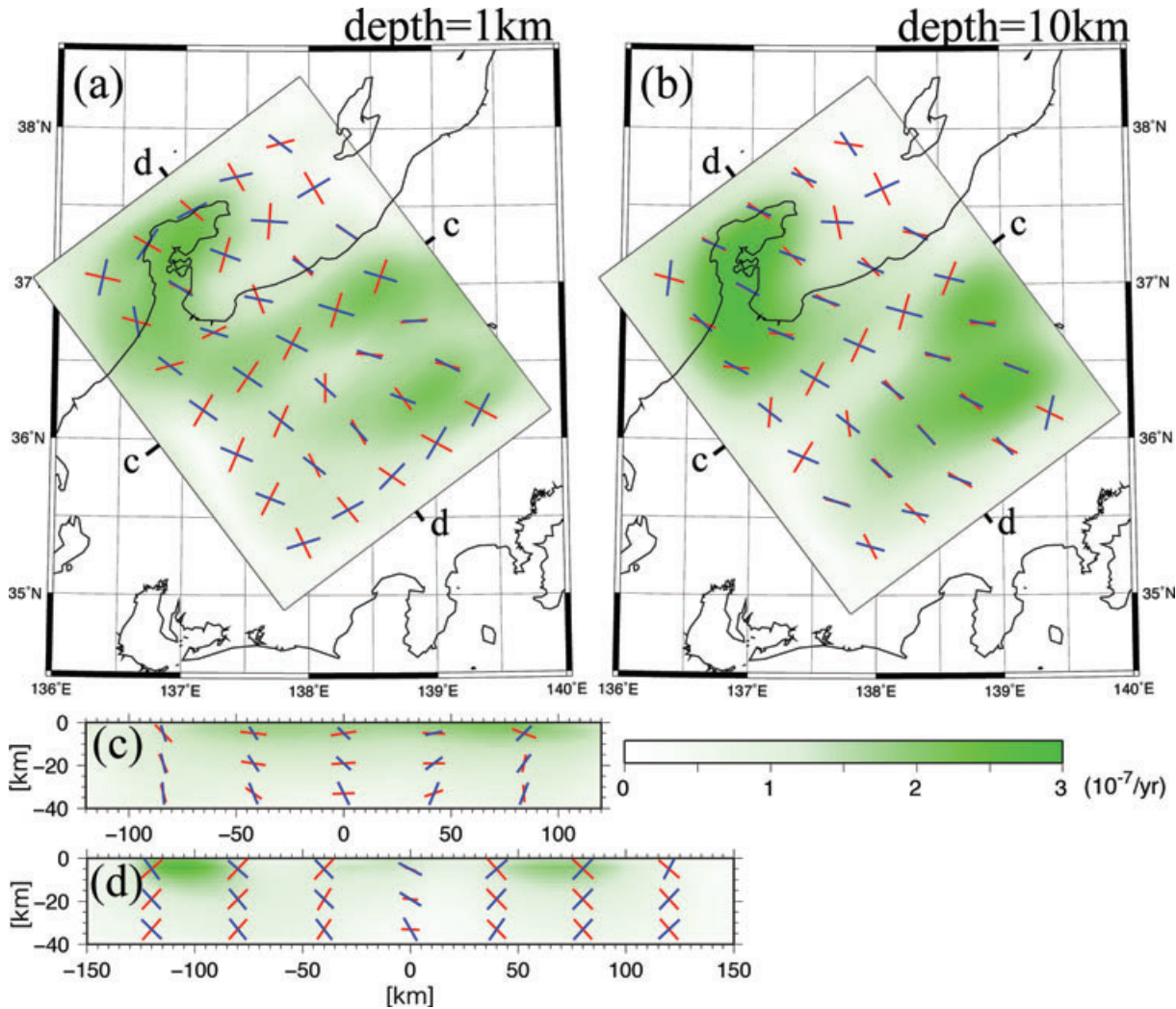


**Figure 7.** The total maximum shear strain rates computed from the optimum moment rate density tensor distribution. The panels (a) and (b) show the horizontal sections at the depths of 1 km and 10 km, respectively. The panels (c) and (d) show the vertical sections along the lines c and d, respectively. The colour-bar scale represents the magnitude of maximum shear strain rate. The red and blue bars indicate the directions of maximum tension and compression, respectively.

side). The distribution of the deviatoric part is rather complex. We can recognize three remarkable shear source regions: a thrust-type shear source region in the northwestern part, a strike-slip-type shear source region in the central part and a thrust-type shear source region in the southeastern part.

To examine the reliability of the inversion results, we calculated the resolution of the optimum moment rate density tensor distribution as follows. The resolution matrix of the optimum model parameters  $\hat{\mathbf{a}}_q$  is defined as

$$\mathbf{R}(\hat{\mathbf{a}}_q) = \mathbf{H}'_q^\dagger \mathbf{H}' = \mathbf{V}_q \mathbf{V}_q^T. \quad (71)$$

The optimum value of moment density tensor  $\delta \hat{\mathbf{m}}$  at a point  $\mathbf{x} = \mathbf{x}_j$  is calculated from the optimum model parameters  $\hat{\mathbf{a}}_q$  by eq. (68) as

$$\delta \hat{\mathbf{m}}(\mathbf{x}_j) = \mathbf{A}(\mathbf{x}_j) \hat{\mathbf{a}}_q, \quad (72)$$

where  $\mathbf{A}(\mathbf{x}_j)$  is a coefficient matrix with its elements of

$$A_{klm}(x_j, y_j, z_j) = T_k\left(\frac{x_j}{X}\right) T_l\left(\frac{y_j}{Y}\right) L_m\left(\frac{z_j}{Z}\right). \quad (73)$$

Then, using the coefficient matrix  $\mathbf{A}$ , we can evaluate the resolution of the optimum moment density tensor distribution at the point

$\mathbf{x} = \mathbf{x}_j$  as

$$\mathbf{R}(\delta \hat{\mathbf{m}}) = \mathbf{A} \mathbf{R}(\hat{\mathbf{a}}_q) \mathbf{A}^T. \quad (74)$$

In the case of perfect resolution, namely  $\mathbf{R}(\hat{\mathbf{a}}_q) = \mathbf{I}$ , the above equation can be written as  $\mathbf{R}(\delta \hat{\mathbf{m}}) = \mathbf{A} \mathbf{A}^T$ . So, we use the normalized resolution,

$$r_j = \sqrt{\left| \frac{[\mathbf{A} \mathbf{R}(\hat{\mathbf{a}}_q) \mathbf{A}^T]_{jj}}{[\mathbf{A} \mathbf{A}^T]_{jj}} \right|}, \quad (75)$$

as an appropriate indicator to represent the resolution of the optimum moment density tensor distribution. In Fig. 5 we show the spatial patterns of the normalized resolution for the isotropic part of moment rate density tensor in Fig. 4(a). From this figure we can see that the present inversion results are reliable in the upper crust ( $-15 \text{ km} \leq z \leq 0 \text{ km}$ ) but not in the lower crust because of the poor resolution.

Given the optimum moment density tensor distribution  $\delta m_{pq}(\xi)$ , we can theoretically compute the internal displacement field  $u_i(\mathbf{x})$  by performing the convolution integral in eq. (11) over the model region  $V$ . The explicit expressions of the spatial derivatives of static Green's tensor  $G_{ip,q}(\mathbf{x}; \xi)$  for a semi-infinite elastic body are given in the Appendix. Then, we numerically differentiate the computed

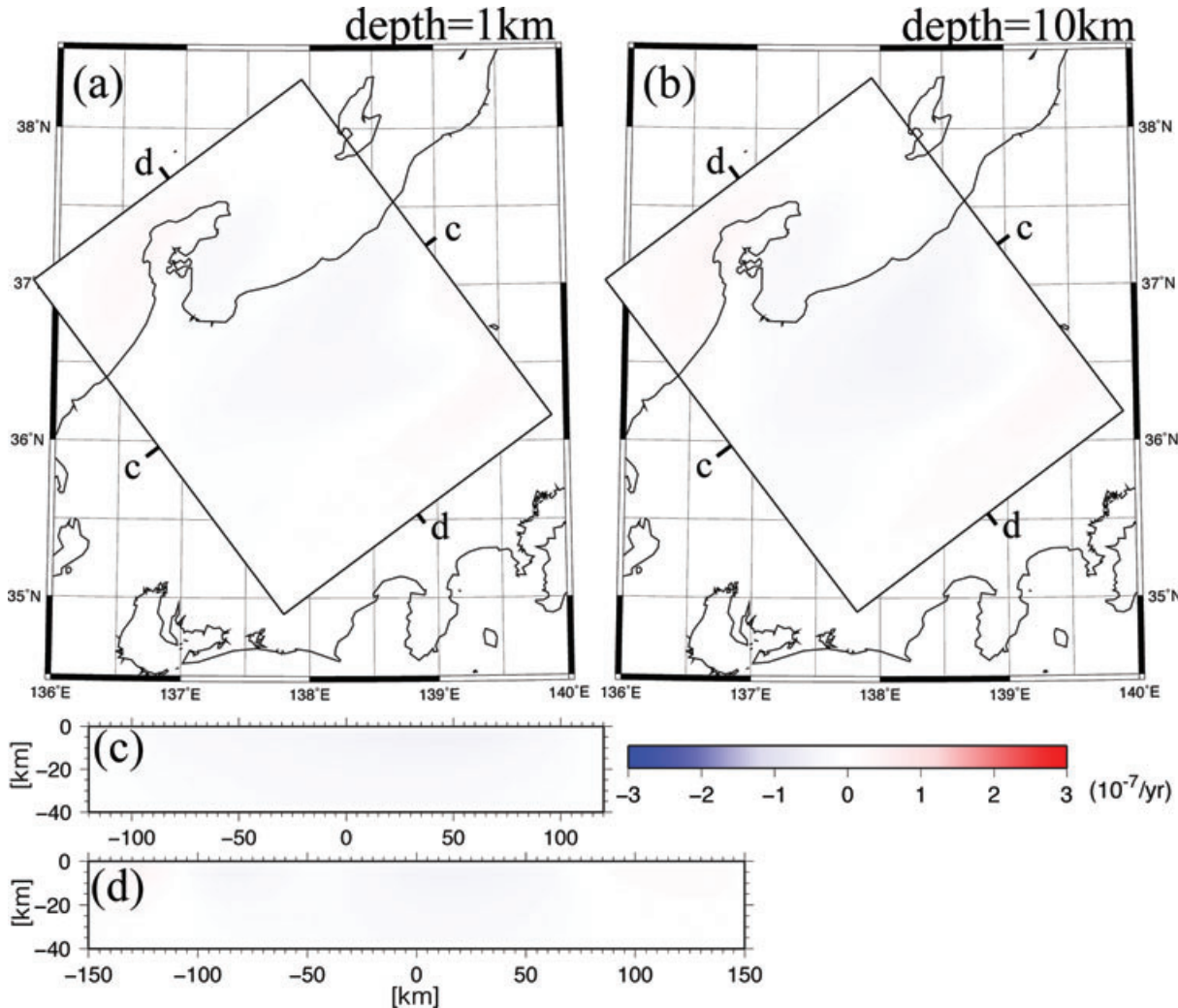


**Figure 8.** The inelastic dilatation rates converted from the isotropic part of the optimum moment rate density tensor. The panels (a) and (b) show the horizontal sections at the depths of 1 km and 10 km, respectively. The panels (c) and (d) show the vertical sections along the lines c and d, respectively. The red and blue of the colour-bar scale indicate dilatation and contraction, respectively.

internal displacement field with respect to spatial coordinates to obtain internal strain fields. Here, it should be noted that the strain obtained by numerically differentiating the displacement field gives total strain (the sum of elastic strain and inelastic strain), because it includes the direct effects of moment density tensor (inelastic strain). As pointed out in Section 2.2, the strain obtained by theoretical computation with analytical strain response functions gives elastic strain, because the analytical strain response functions are not defined at source points. We show the total strain rate fields in Fig. 6 for dilatation and in Fig. 7 for maximum shear strain with the same colour-bar scale. From these figures we can recognize the existence of a remarkable contraction region localized in the uppermost crust and two remarkable shear regions spreading over the upper crust.

On the other hand, using eq. (14), we can directly obtain inelastic strain rate fields from the inverted moment rate density tensor distribution. We show the inelastic strain rate fields in Fig. 8 for dilatation and in Fig. 9 for maximum shear strain with the same colour-bar scale as in Figs 6 and 7. The amplitude of inelastic dilatation rates in Fig. 8 is much smaller than that of total dilatation rates in Fig. 6, and so the patterns of inelastic dilatation rates are almost invisible

on this colour-bar scale. The inelastic maximum shear strain rate fields in Fig. 9 show a similar pattern and amplitude to the total maximum shear strain rate fields in Fig. 7. Subtracting the inelastic strain rates in Figs 8 and 9 from the total strain rates in Figs 6 and 7, respectively, we can obtain the elastic strain rate fields, which are shown in Fig. 10 for dilatation and in Fig. 11 for maximum shear strain with the same colour-bar scale as in Figs 6 and 7. The elastic dilatation rate fields in Fig. 10 show a similar pattern and amplitude to the total dilatation rate fields in Fig. 6. The amplitude of elastic maximum shear strain rates in Fig. 11 is much smaller than that of the total maximum shear strain rates in Fig. 7, and so the patterns of elastic maximum shear strain rates are almost invisible on this colour-bar scale.

From almost the same GPS velocity data, Sagiya *et al.* (2000) have estimated the horizontal strain rates of Japanese Islands, including the Niigata–Kobe transformation zone, with the 2-D geometric inversion method by Shen *et al.* (1996). The strain obtained from the geometric analysis of GPS data are total strain at the Earth's surface, and so we can directly compare the surface patterns of dilatation and maximum shear strain rates in Figs 6(a) and 7(a) with their results. As far as the surface pattern of total strain is

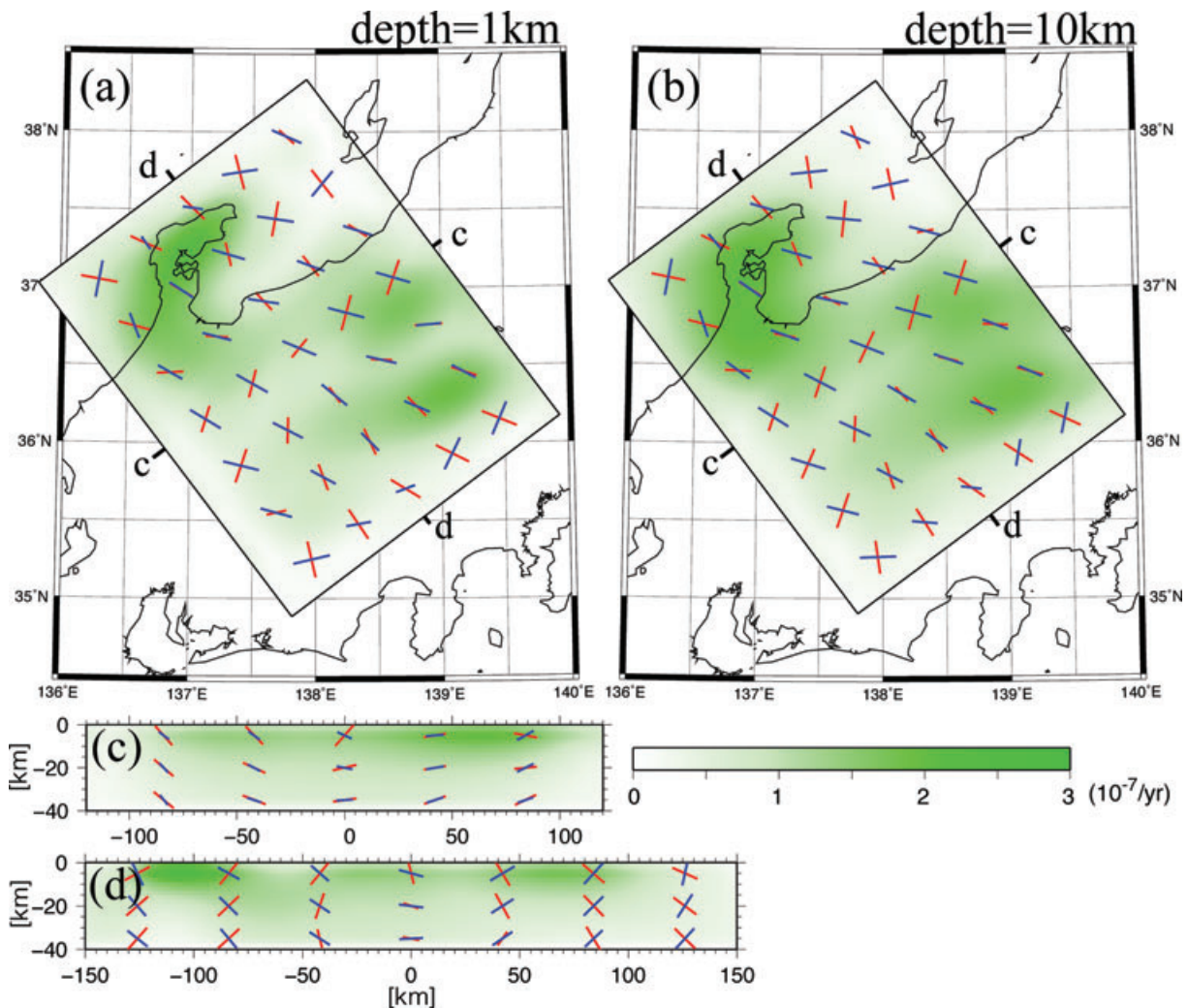


**Figure 9.** The inelastic maximum shear strain rates converted from the deviatoric part of the optimum moment rate density tensor. The panels (a) and (b) show the horizontal sections at the depths of 1 km and 10 km, respectively. The panels (c) and (d) show the vertical sections along the lines c and d, respectively. The colour-bar scale represents the magnitude of maximum shear strain rate. The red and blue bars indicate the directions of maximum tension and compression, respectively.

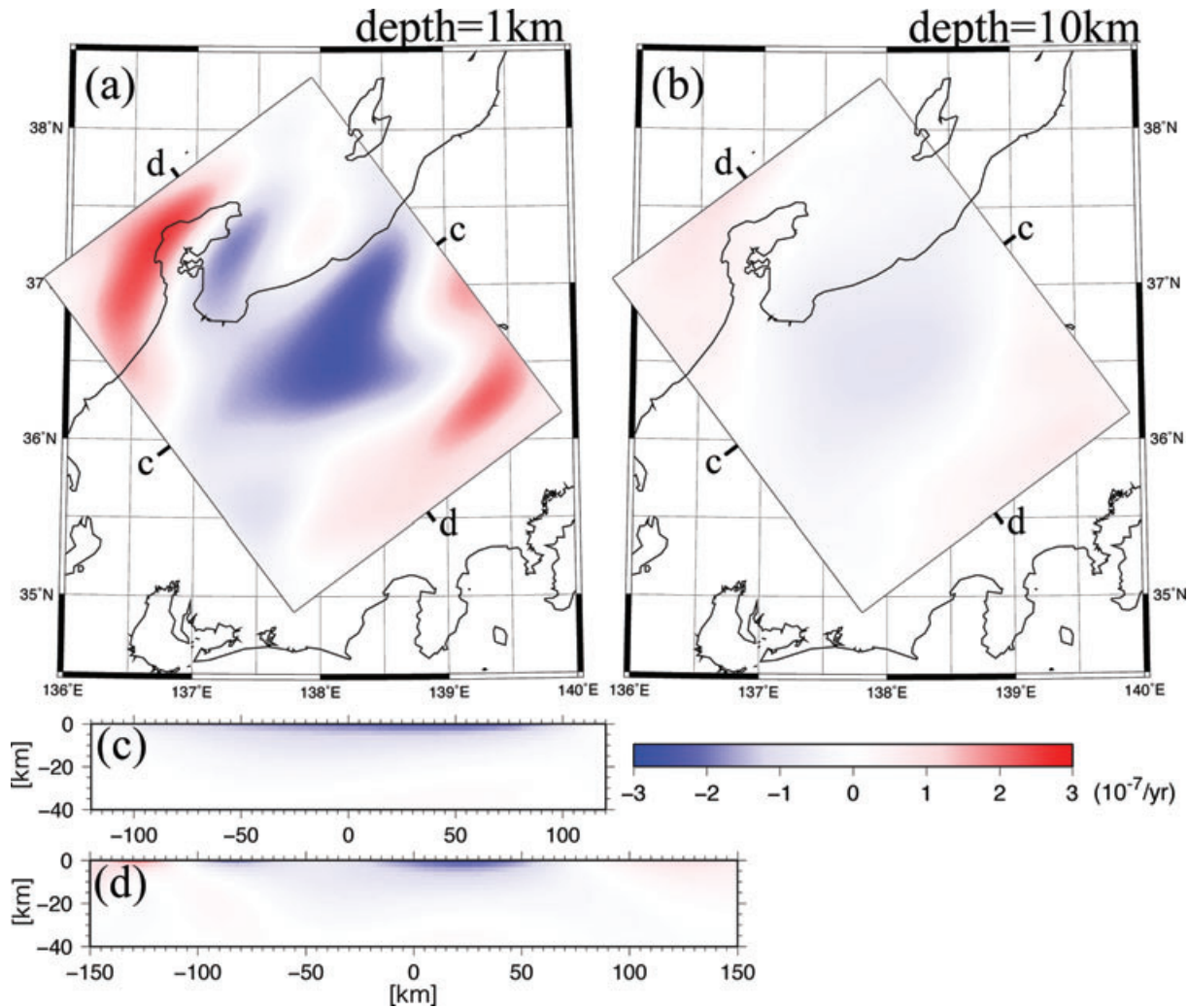


**Figure 10.** The elastic dilatation rates obtained by subtracting the inelastic part from the total dilatation rates. The panels (a) and (b) show the horizontal sections at the depths of 1 km and 10 km, respectively. The panels (c) and (d) show the vertical sections along the lines c and d, respectively. The red and blue of the colour-bar scale indicate dilatation and contraction, respectively.

concerned, our results of 3-D physics based inversion analysis accord with their results of 2-D geometric inversion analysis. However, from the comparison of Figs 6, 8 and 10, we can see that the remarkable contraction observed in the Niigata–Kobe transformation zone is almost elastic and restricted near the Earth’s surface. From the comparison of Figs 7, 9 and 11, on the other hand, we can see that the remarkable shear deformation observed is almost inelastic and extends over the upper crust.

## 5 DISCUSSION

In Section 2, representing the sources that deform the Earth’s crust by spatiotemporally distributed moment tensors, we created a theory of physics-based strain analysis. In Section 3, on the theory of physics-based strain analysis, we mathematically formulated the inversion method to separately estimate 3-D elastic and inelastic strain fields from GPS array data. This method can be regarded as a general extension of ordinary geodetic data inversion methods to estimate fault slip or slip-deficit distribution on a known internal surface such as active faults and plate interfaces.

Given the location and geometry of a plate interface  $\Sigma(\boldsymbol{\eta})$  and the direction of fault slip  $\boldsymbol{\nu}(\boldsymbol{\eta})$ , for example, we can represent fault slip

vectors  $\delta\mathbf{w}(\boldsymbol{\eta})$  at the plate interface as

$$\delta\mathbf{w}(\boldsymbol{\eta}) = \delta w(\boldsymbol{\eta})\boldsymbol{\nu}(\boldsymbol{\eta}), \quad (76)$$

where  $\delta w$  is the magnitude of fault slip. By using the Dirac delta function  $\delta(\boldsymbol{\xi} - \boldsymbol{\eta})$ , the inelastic strain accompanied by the fault slip  $\delta\mathbf{w}$  at the plate interface  $\Sigma$  is represented as

$$\delta\varepsilon_{kl}^a(\boldsymbol{\xi}) = \delta w(\boldsymbol{\eta})v_k(\boldsymbol{\eta})n_l(\boldsymbol{\eta})\delta(\boldsymbol{\xi} - \boldsymbol{\eta}), \quad (77)$$

where  $\mathbf{n}(\boldsymbol{\eta})$  denotes the unit normal vector of  $\Sigma$ . So, from eq. (10), the corresponding moment density tensor is given by

$$\delta m_{ij}(\boldsymbol{\xi}) \equiv c_{ijkl}\delta\varepsilon_{kl}^a(\boldsymbol{\xi}) = \delta m_{ij}^\Sigma(\boldsymbol{\eta})\delta(\boldsymbol{\xi} - \boldsymbol{\eta}), \quad (78)$$

with

$$\delta m_{ij}^\Sigma(\boldsymbol{\eta}) = c_{ijkl}\delta w(\boldsymbol{\eta})v_k(\boldsymbol{\eta})n_l(\boldsymbol{\eta}). \quad (79)$$

That is to say, the fault slip at a plate interface is represented by the distribution of moment density tensor localized at the plate interface (Backus & Mulcahy 1976b). Substituting eq. (78) into eq. (11), we obtain the expressions of surface displacements  $u_i(\mathbf{x})$  due to the

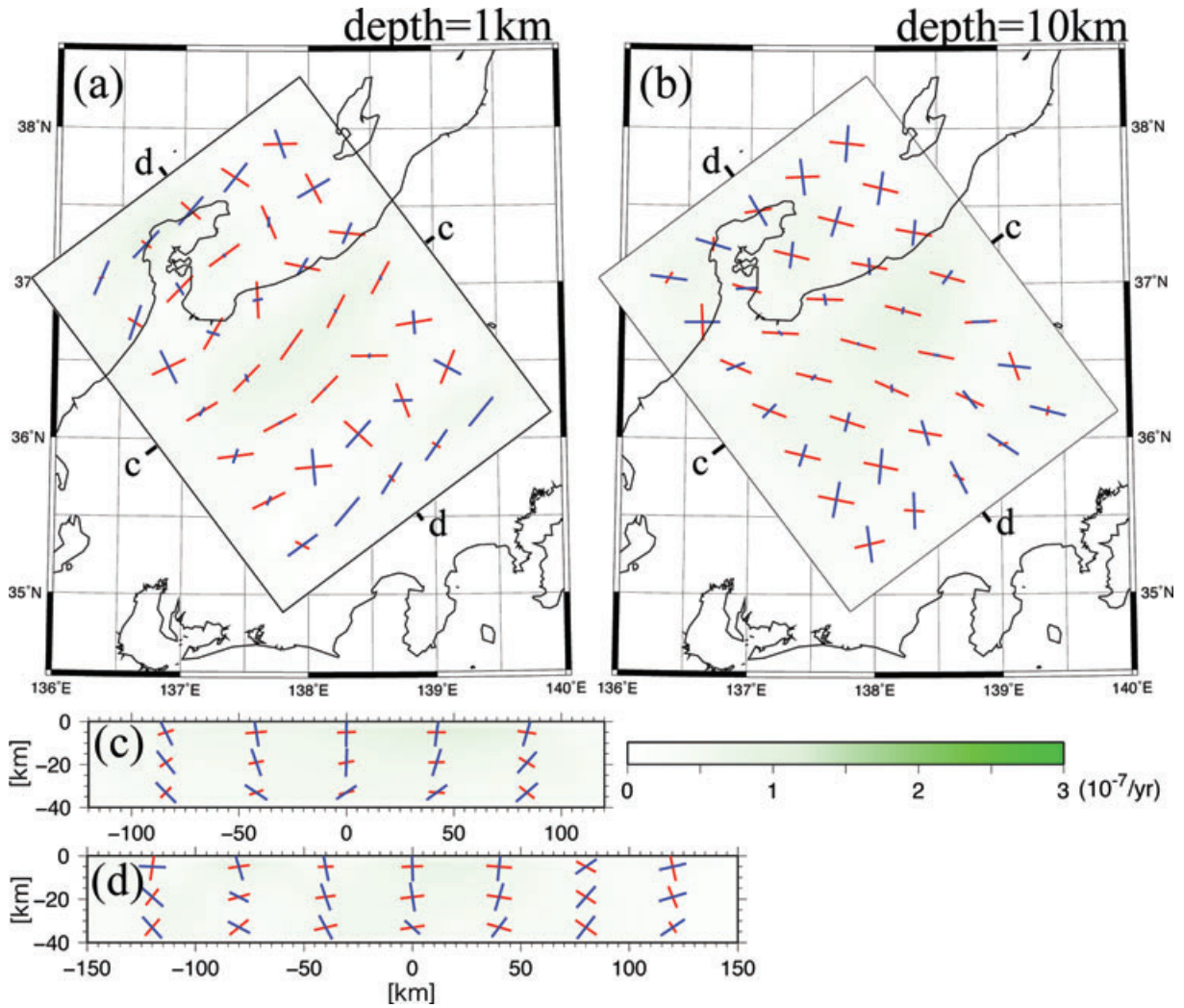


**Figure 11.** The elastic maximum shear strain rates obtained by subtracting the inelastic part from the total maximum shear strain rates. The panels (a) and (b) show the horizontal sections at the depths of 1 km and 10 km, respectively. The panels (c) and (d) show the vertical sections along the lines c and d, respectively. The colour-bar scale represents the magnitude of maximum shear strain rate. The red and blue bars indicate the directions of maximum tension and compression, respectively.

fault slip at the plate interface as

$$\begin{aligned} u_i(\mathbf{x}) &= \int_{\Sigma} G_{ip,q}(\mathbf{x}; \boldsymbol{\eta}) \delta m_{pq}^{\Sigma}(\boldsymbol{\eta}) d\Sigma \\ &= \int_{\Sigma} G_{ip,q}(\mathbf{x}; \boldsymbol{\eta}) c_{pqkl} v_k(\boldsymbol{\eta}) n_l(\boldsymbol{\eta}) \delta w(\boldsymbol{\eta}) d\Sigma. \end{aligned} \quad (80)$$

Given surface displacement data, we can solve the above equations for  $\delta w(\boldsymbol{\eta})$ . This is the ordinary geodetic data inversion to estimate fault slip distribution. As for the ordinary geodetic data inversion, Matsu'ura *et al.* (2007) have developed a general method based on Bayesian modelling with direct and indirect prior information.

In plate boundary zones, the crustal deformation is caused partly by fault slip and/or slip-deficit at plate interfaces  $\Sigma$  and partly by brittle fracture and/or plastic flow at the defects distributed in the surrounding crustal region  $V$ ; that is,

$$u_i(\mathbf{x}) = \int_{\Sigma} G_{ip,q}(\mathbf{x}; \boldsymbol{\eta}) \delta m_{pq}^{\Sigma}(\boldsymbol{\eta}) d\Sigma + \int_V G_{ip,q}(\mathbf{x}; \boldsymbol{\xi}) \delta m_{pq}(\boldsymbol{\xi}) dV. \quad (81)$$

Therefore, to analyse geodetic data in plate boundary zones, we need to combine the ordinary inversion method for  $\delta m_{pq}^{\Sigma}(\boldsymbol{\eta})$  and the present inversion method for  $\delta m_{pq}(\boldsymbol{\xi})$  in a unified way.

In Section 4, we revealed 3-D elastic and inelastic strain rate fields in the Niigata–Kobe transformation zone by applying the inversion method to GPS horizontal velocity data. Given the elastic and inelastic strain fields individually, we can evaluate the mechanical properties of the crust in the following way. First, we decompose the total strain tensor  $\varepsilon_{ij}(\mathbf{x})$ , which is the sum of elastic strain  $\varepsilon_{ij}^e(\mathbf{x})$  and inelastic strain  $\varepsilon_{ij}^a(\mathbf{x})$ , into its isotropic part  $\varepsilon_{kk}(\mathbf{x})$  and deviatoric part  $\varepsilon'_{ij}(\mathbf{x})$ :

$$\varepsilon_{kk}(\mathbf{x}) = \varepsilon_{kk}^e(\mathbf{x}) + \varepsilon_{kk}^a(\mathbf{x}), \quad (82)$$

$$\varepsilon'_{ij}(\mathbf{x}) = \varepsilon_{ij}^e(\mathbf{x}) + \varepsilon_{ij}^a(\mathbf{x}) \quad (83)$$

with

$$\varepsilon'_{ij} = \varepsilon_{ij} - \frac{1}{3} \varepsilon_{kk} \delta_{ij}, \quad \varepsilon_{ij}^e = \varepsilon_{ij} - \frac{1}{3} \varepsilon_{kk}^e \delta_{ij}, \quad \varepsilon_{ij}^a = \varepsilon_{ij}^a - \frac{1}{3} \varepsilon_{kk}^a \delta_{ij}. \quad (84)$$

We also decompose the stress tensor  $\sigma_{ij}(\mathbf{x})$  into its isotropic part  $\sigma_{kk}(\mathbf{x})$  and deviatoric part:

$$\sigma'_{ij}(\mathbf{x}) = \sigma_{ij}(\mathbf{x}) - \frac{1}{3} \sigma_{kk}(\mathbf{x}) \delta_{ij}. \quad (85)$$

Then, denoting the rigidity and bulk modulus of a reference elastic body by  $\bar{\mu}$  and  $\bar{\kappa}$ , respectively, we can obtain the relation between the deviatoric stress and the deviatoric strain as

$$\sigma'_{ij}(\mathbf{x}) = 2\bar{\mu}\varepsilon'_{ij}(\mathbf{x}) = 2\mu^*(\mathbf{x})\varepsilon'_{ij}(\mathbf{x}) \quad (86)$$

with

$$\mu^*(\mathbf{x}) = \frac{\varepsilon'_{ij}(\mathbf{x})}{\varepsilon'_{ij}(\mathbf{x}) + \varepsilon'_{ij}(\mathbf{x})} \bar{\mu}. \quad (87)$$

Here,  $\mu^*(\mathbf{x})$  represents the effective rigidity based on the concept of damage rheology.

In a similar way, we can obtain the relation between the isotropic part of stress and the isotropic part of strain as

$$\sigma_{kk}(\mathbf{x}) = 3\bar{\kappa}\varepsilon_{kk}(\mathbf{x}) = 3\kappa^*(\mathbf{x})\varepsilon_{kk}(\mathbf{x}) \quad (88)$$

with

$$\kappa^*(\mathbf{x}) = \frac{\varepsilon_{kk}(\mathbf{x})}{\varepsilon_{kk}(\mathbf{x}) + \varepsilon_{kk}(\mathbf{x})} \bar{\kappa}. \quad (89)$$

However, since the generation of inelastic isotropic strain  $\varepsilon_{kk}^a$  is limited to the case of thermal expansion and/or phase change, the effective bulk modulus  $\kappa^*(\mathbf{x})$  must be almost equal to the reference bulk modulus  $\bar{\kappa}$  in the normal regions of the upper crust.

From the inversion results in Section 4.3, we evaluated the effective rigidity and effective bulk modulus in the Niigata–Kobe transformation zone. Figs 12(a) and (b) show the surface patterns of effective rigidity and effective bulk modulus, respectively. From Fig. 12(b) we can see that the effective bulk modulus changes little from the reference bulk modulus  $\bar{\kappa}$ . This result is consistent with that the observed horizontal contraction near the surface is elastic. From Fig. 12(a), on the other hand, we can see that the effective

rigidity is much smaller than the reference rigidity  $\bar{\mu}$  in the same region. This result indicates that the dominant deformation mode in the upper crust is inelastic shear without volume change. Now, a question arises as to the mechanism of the abnormal elastic horizontal contraction near the surface. We may interpret the elastic horizontal contraction as the secondary deformation of a surface sedimentary layer caused by the inelastic shear deformation in the deeper part of the crust. If the surface sedimentary layer has poroelastic properties, it would macroscopically behave like an elastic body with abnormally small bulk modulus.

## 6 CONCLUSIONS

The Earth's crust, which is macroscopically treated as a linear elastic body, includes a number of defects. The occurrence of inelastic deformation such as brittle fracture and/or plastic flow at the defects brings about elastic deformation in the surrounding regions. Representing the brittle fracture and/or plastic flow by moment density tensor distribution, we created a theory of physics-based strain analysis, and developed an inversion method to separately estimate 3-D elastic and inelastic strain fields from GPS data. In this method, first, we determine the optimum distribution of moment density tensor from observed GPS data by using AIC. Converting the optimum moment density tensor distribution with elastic compliance tensor, we can directly obtain 3-D inelastic strain fields. On the other hand, given the optimum moment density tensor distribution, we can theoretically compute 3-D elastic strain fields. The strain obtained by conventional geometric analysis is only the 2-D horizontal components of unseparated total strain. We applied the inversion method to GPS horizontal velocity data (1996–2000) in the Niigata–Kobe

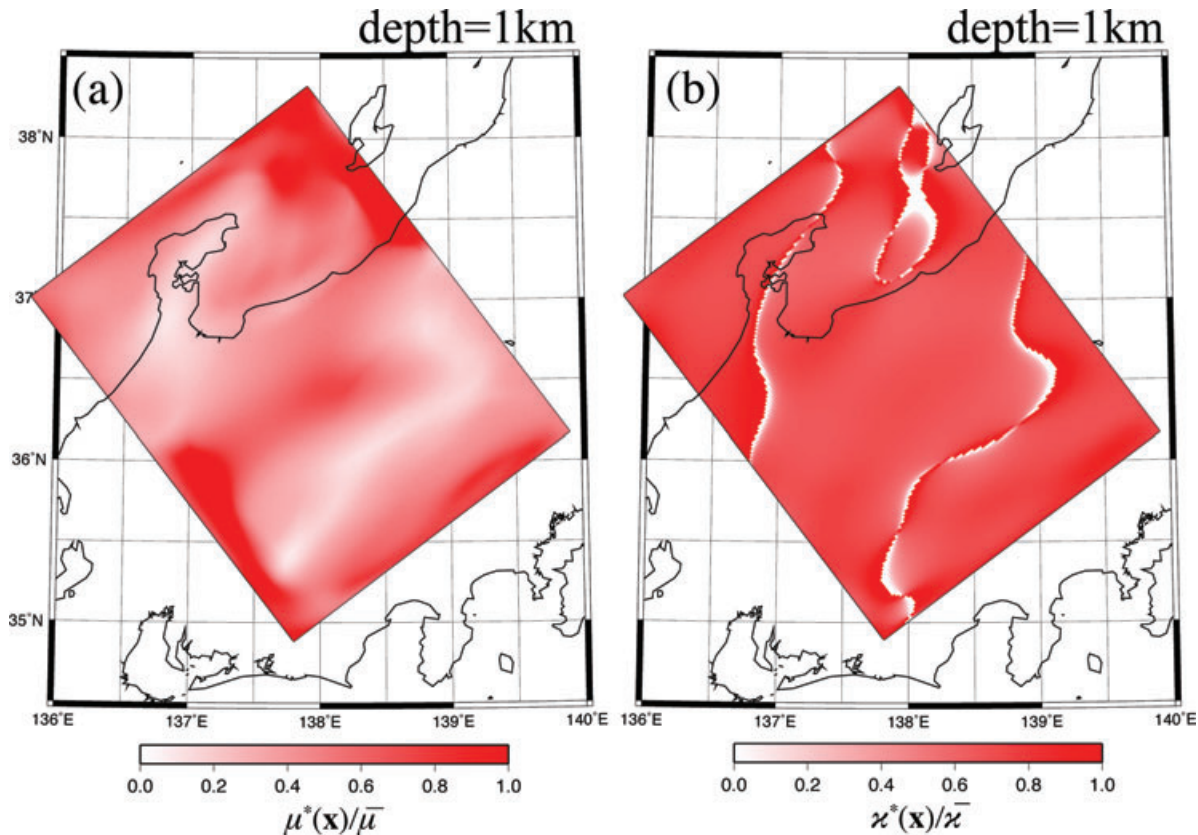


**Figure 12.** The horizontal patterns of effective rigidity and effective bulk modulus at the surface: (a) the ratio of effective rigidity to reference rigidity and (b) the ratio of effective bulk modulus to reference bulk modulus.



transformation zone, central Japan, and succeeded in estimating 3-D elastic and inelastic strain rate fields separately. As for the surface patterns of total strain rates, the results of 3-D physics based inversion analysis accord with the results of 2-D geometric inversion analysis by Sagiya *et al.* (2000). From the 3-D patterns of the inverted elastic and inelastic strain fields, we revealed that the remarkable horizontal contraction in the Niigata–Kobe transformation zone is elastic and restricted near the surface, but the remarkable shear deformation is inelastic and extends over the upper crust.

## ACKNOWLEDGMENTS

We thank Takeshi Sagiya for permitting us to use GPS velocity data (1996–2000) in Japan for the present inversion analysis. We also thank the anonymous reviewers for their thoughtful comments.

## REFERENCES

- Akaike, H., 1974. A new look at the statistical model identification, *IEEE Trans. Autom. Contr.*, **19**, 716–723.
- Akaike, H., 1977. On entropy maximization principle, in *Application of Statistics*, pp. 27–41, ed. Krishnaiah, P.R., North-Holland, Amsterdam.
- Backus, G. & Mulcahy, M., 1976a. Moment tensors and other phenomenological descriptions of seismic sources—I. Continuous displacements, *Geophys. J. R. astr. Soc.*, **46**, 341–361.
- Backus, G. & Mulcahy, M., 1976b. Moment tensors and other phenomenological descriptions of seismic sources—II. Discontinuous displacements, *Geophys. J. R. astr. Soc.*, **47**, 301–329.
- De Berg, M., van Kreveld, M., Overmars, M. & Schwarzkopf, O., 1997. *Computational Geometry: Algorithm and Applications*, pp. 191–218, Springer-Verlag, Berlin.
- El-Fiky, G.S. & Kato, T., 1999. Continuous distribution of the horizontal strain in the Tohoku district, Japan, predicted by least-squares collocation, *Geodynamics*, **27**, 213–236.
- El-Fiky, G.S. & Kato, T., 2006. Secular crustal deformation and interplate coupling of the Japanese Islands as deduced from continuous GPS array, 1996–2001, *Tectonophysics*, **422**, 1–22.
- Frank, F.C., 1966. Deduction of earth strains from survey data, *Bull. seism. Soc. Am.*, **56**, 35–42.
- Fung, Y.C., 1965. *Foundations of Solid Mechanics*, pp. 89–115, Prentice-Hall, Englewood Cliffs, NJ.
- Haines, A.J., 1982. Calculating velocity fields across plate boundaries from observed shear rates, *Geophys. J. R. astr. Soc.*, **68**, 203–209.
- Haines, A.J. & Holt, W.E., 1993. A procedure for obtaining the complete horizontal motions within zones of distributed deformation from the inversion of strain rate data, *J. geophys. Res.*, **98**, 12 057–12 082.
- Hashima, A., Takada, Y., Fukahata, Y. & Matsu'ura, M., 2008. General expressions for internal deformation due to a moment tensor in an elastic/viscoelastic multilayered half-space, *Geophys. J. Int.*, **175**, 992–1012.
- Hashimoto, C., Fukui, K. & Matsu'ura, M., 2004. 3-D modeling of plate interfaces and numerical simulation of long-term crustal deformation in and around Japan, *Pure appl. Geophys.*, **161**, 2053–2068.
- Hashimoto, C., Noda, A., Sagiya, T. & Matsu'ura, M., 2009. Interplate seismogenic zones along the Kuril–Japan trench inferred from GPS data inversion, *Nature Geoscience*, **2**, 141–144.
- Hofmann-Wellenhof, B. & Moritz, H., 2005. *Physical Geodesy*, 2nd edn, pp. 173–238, Springer-Verlag, New York.
- Holt, W.E. & Haines, A.J., 1993. Velocity fields in deforming Asia from the inversion of earthquake-release strains, *Tectonics*, **12**, 1–20.
- Jackson, D.D., 1972. Interpretation of inaccurate, insufficient and inconsistent data, *Geophys. J. Roy. Astr. Soc.*, **28**, 97–109.
- Jackson, J.A. & McKenzie, D., 1988. The relationship between plate motions and seismic moment tensors, and the rates of active deformation in the Mediterranean and Middle East, *Geophys. J. Roy. Astr. Soc.*, **93**, 45–73.

- Kato T., El-Fiky, G.S., Oware, E.N. & Miyazaki, S., 1998. Crustal strains in the Japanese islands as deduced from dense GPS array, *Geophys. Res. Lett.*, **25**, 3445–3448.
- Kostrov, B.V., 1974. Seismic moment and energy of earthquakes, and seismic flow of rock, *Izvestia, Phys. Solid Earth, Engl. Transl.*, **10**, 13–21.
- Lanczos, C., 1961. *Linear Differential Operators*, pp. 100–162, Van Nostrand, London.
- Matsu'ura, M., Noda, A. & Fukahata, Y., 2007. Geodetic data inversion based on Bayesian formulation with direct and indirect prior information, *Geophys. J. Int.*, **171**, 1342–1351.
- Mazzotti, S., Henry, P. & Le Pichon, X., 2001. Transient and permanent deformation of central Japan estimated by GPS: 2. Strain partitioning and arc-arc collision, *Earth planet. Sci. Lett.*, **184**, 455–469.
- Okada, Y., 1992. Internal deformation due to shear and tensile faults in a half-space, *Bull. seism. Soc. Am.*, **82**, 1018–1040.
- Press, F., 1965. Displacements, strains and tilts at teleseismic distances, *J. geophys. Res.*, **70**, 2395–2412.
- Reilly, W.I., 2003. Strain in the Earth: a geodetic perspective, in *Geodesy—The Challenge of the 3rd Millennium*, pp. 455–462, eds Grafarend, E.W., Krumm, F.W. & Schwarze, V.S., Springer-Verlag, Berlin.
- Sagiya, T., 2004. Interplate coupling in the Kanto district, central Japan, and the Boso peninsula silent earthquake in May 1996, *Pure appl. Geophys.*, **161**, 2327–2342.
- Sagiya, T., Miyazaki, S. & Tada, T., 2000. Continuous GPS array and present-day crustal deformation of Japan, *Pure appl. Geophys.*, **157**, 2303–2322.
- Shen, Z.-K., Jackson, D.D. & Ge, B.X., 1996. Crustal deformation across and beyond the Los Angeles basin from geodetic measurements, *J. geophys. Res.*, **101**, 27 957–27 980.
- Shen-Tu, B., Holt, W.E. & Haines, A.J., 1995. Intraplate deformation in the Japanese Islands: a kinematic study of intraplate deformation at a convergent plate margin, *J. geophys. Res.*, **100**, 24275–24293.
- Townend, J. & Zoback, M.D., 2006. Stress, strain, and mountain building in central Japan, *J. geophys. Res.*, **111**, B03411, doi:10.1029/2005JB003759.
- Tsuboi, C., 1932. Investigation on the deformation of the Earth's crust in Idu Peninsula connected with the Idu earthquake of Nov. 26, 1930, *Bull. Earthq. Res. Inst., Univ. Tokyo*, **10**, 435–448.
- Twiss, R.J. & Unruh, J.R., 1998. Analysis of fault slip inversion: do they constrain stress or strain rate?, *J. geophys. Res.*, **103**, 12 205–12 222.
- Wesnousky, S.G., Scholz, C.H. & Shimazaki, K., 1982. Deformation of island arc: rates of moment release and crustal shortening in intraplate Japan determined from seismicity and Quaternary fault data, *J. geophys. Res.*, **87**, 6829–6852.
- Wiggins, R.A., 1972. The general linear inverse problem: implication of surface waves and free oscillations for Earth structure, *Rev. Geophys. Space Phys.*, **10**, 251–285.
- Yabuki, T. & Matsu'ura, M., 1992. Geodetic data inversion using a Bayesian information criterion for spatial distribution of fault slip, *Geophys. J. Int.*, **109**, 363–375.

## APPENDIX: DISPLACEMENT FIELDS DUE TO A MOMENT TENSOR IN ELASTIC HALF-SPACE

We consider an elastic body with Lamé's constants  $\lambda$  and  $\mu$ , occupying the negative  $x_3$  region of a Cartesian coordinates  $(x_1, x_2, x_3)$ . Denoting the coordinates of a calculation point by  $\mathbf{x} = (x_1, x_2, x_3)$  with  $x_3 \leq 0$  and the coordinates of a source point by  $\boldsymbol{\xi} = (\xi_1, \xi_2, \xi_3)$  with  $\xi_3 < 0$ , we can generally represent the internal displacement field due to moment density tensor distribution  $m_{pq}(\boldsymbol{\xi})$  as

$$u_i(\mathbf{x}) = \sum_{p=1}^3 \sum_{q=1}^3 \int_V G_{ip,q}(\mathbf{x}; \boldsymbol{\xi}) m_{pq}(\boldsymbol{\xi}) dV \quad (i = 1, 2, 3), \quad (\text{A1})$$

where  $G_{ip,q}(\mathbf{x}; \boldsymbol{\xi})$  are the partial derivatives of static Green's tensor  $G_{ip}$  with respect to the source coordinate  $\xi_q$ . The analytic expressions for the internal displacement field due to a single force

(static Green's tensor  $G_{ip}$ ) are given in Press (1965). Differentiating these expressions with respect to the source coordinate, we obtain the expressions for the spatial derivatives  $G_{ip,q}(\mathbf{x}; \boldsymbol{\xi})$  of static Green's tensor (Okada, 1992).

The spatial derivatives of static Green's tensor are calculated as the sum of four terms:

$$G_{ip,q}(\mathbf{x}; \boldsymbol{\xi}) = G_{ip,q}^A(\mathbf{x}; \boldsymbol{\xi}) - G_{ip,q}^A(\mathbf{x}^-; \boldsymbol{\xi}) + G_{ip,q}^B(\mathbf{x}^-; \boldsymbol{\xi}) + G_{ip,q}^C(\mathbf{x}^-; \boldsymbol{\xi}), \quad (\text{A2})$$

where  $\mathbf{x}^- = (x_1, x_2, -x_3)$  indicates the change in sign of the  $x_3$ -coordinate of the calculation point  $\mathbf{x} = (x_1, x_2, x_3)$ . The explicit expressions for the above four terms are given by

$$G_{ip,q}^A = \frac{1}{8\pi\mu} \frac{1}{\gamma + 1} \frac{1}{R^2} [3R_i R_p R_q - R_i \delta_{pq} - R_p \delta_{iq} + (2\gamma + 1)R_q \delta_{ip}], \quad (\text{A3})$$

$$G_{ip,q}^B = \frac{1}{4\pi\mu} \frac{1}{R^2} \left\{ (3R_i R_p R_q - R_i \delta_{pq} - R_p \delta_{iq} + R_q \delta_{ip}) + \gamma \left[ \frac{(R_q + \delta_{q3})\delta_{ip}}{(1 + R_3)^2} - \frac{\delta_{iq} \delta_{p3} - \delta_{pq} \delta_{i3}(1 - \delta_{p3})}{(1 + R_3)} + [R_i \delta_{p3} - R_p \delta_{i3}(1 - \delta_{p3})] \frac{\delta_{q3} + R_q(2 + R_3)}{(1 + R_3)^2} + (1 - \delta_{i3})(1 - \delta_{p3}) \left( \frac{R_i \delta_{pq} + R_p \delta_{iq}}{(1 + R_3)^2} - R_i R_p \frac{2\delta_{q3} + R_q(3 + R_3)}{(1 + R_3)^3} \right) \right] \right\}, \quad (\text{A4})$$

$$G_{ip,q}^C = \frac{1}{4\pi\mu} \frac{1}{\gamma + 1} \frac{1}{R^3} (1 - 2\delta_{i3}) \{ (2\gamma + 1)[(\delta_{pq} - 3R_p R_q)\delta_{i3} - (\delta_{iq} - 3R_i R_q)\delta_{p3}] + [(\delta_{ip} - 3R_i R_p)\delta_{q3} + 3Z(R_i \delta_{pq} + R_p \delta_{iq} + R_q \delta_{ip} - 5R_i R_p R_q)] \}. \quad (\text{A5})$$

Here,  $R$  is the distance between the source point  $\boldsymbol{\xi}$  and the calculation point  $\mathbf{x}$ , defined by

$$R = \sqrt{X_1^2 + X_2^2 + X_3^2} \quad (\text{A6})$$

with

$$X_i = x_i - \xi_i \quad (i = 1, 2, 3), \quad (\text{A7})$$

and  $R_i$  is the  $i$ th component of the unit vector pointing from  $\boldsymbol{\xi}$  to  $\mathbf{x}$ , defined by

$$R_i = X_i / R \quad (i = 1, 2, 3). \quad (\text{A8})$$

$Z$  (a source-depth dependent variable) and  $\gamma$  (a material constant) are defined by

$$Z = \xi_3 / R \quad (\text{A9})$$

and

$$\gamma = \mu / (\lambda + \mu). \quad (\text{A10})$$